

# Annelid functional genomics reveal the origins of bilaterian life cycles

**Jose Martín-Durán** (✉ [chema.martin@qmul.ac.uk](mailto:chema.martin@qmul.ac.uk))

Queen Mary University of London <https://orcid.org/0000-0002-2572-1061>

**Yan Liang**

Queen Mary University of London

**Francisco M. Martín-Zamora**

Queen Mary University of London <https://orcid.org/0000-0002-2558-3762>

**Kero Guynes**

Queen Mary University of London

**Allan Carrillo-Baltodano**

Queen Mary University of London

**Yongkai Tan**

Okinawa Institute of Science and Technology Graduate University

**Giacomo Moggioli**

Queen Mary University of London

**Oceane Seudre**

Queen Mary University of London

**Martin Tran**

Queen Mary University of London

**Kate Martimer**

Amgueddfa Cymru – National Museum Wales

**Nicholas Luscombe**

Okinawa Institute of Science and Technology Graduate University

**Andreas Hejnol**

University of Bergen <https://orcid.org/0000-0003-2196-8507>

**Ferdinand Marlétaz**

University College London

---

**Biological Sciences - Article**

**Keywords:**

**Posted Date:** February 15th, 2022

**DOI:** <https://doi.org/10.21203/rs.3.rs-1347136/v1>

**License:**  This work is licensed under a Creative Commons Attribution 4.0 International License.

[Read Full License](#)

---

# 1 **Annelid functional genomics reveal the origins of bilaterian life cycles**

2 Yan Liang<sup>1,§</sup>, Francisco M. Martín-Zamora<sup>1,§</sup>, Kero Guynes<sup>1</sup>, Allan M. Carrillo-Baltodano<sup>1</sup>,  
3 Yongkai Tan<sup>2</sup>, Giacomo Moggioli<sup>1</sup>, Océane Seudre<sup>1</sup>, Martin Tran<sup>1,3</sup>, Kate Mortimer<sup>4</sup>,  
4 Nicholas M. Luscombe<sup>2</sup>, Andreas Hejnol<sup>5,6</sup>, Ferdinand Marlétaz<sup>7,8,\*</sup>, José M. Martín-Durán<sup>1,\*</sup>

5  
6 <sup>1</sup>School of Biological and Behavioural Sciences, Queen Mary University of London, London,  
7 United Kingdom

8 <sup>2</sup>Genomics and Regulatory Systems Unit, Okinawa Institute of Science and Technology  
9 Graduate University, Okinawa, Japan

10 <sup>3</sup>Department of Infectious Disease, Imperial College London, London, United Kingdom

11 <sup>4</sup>Department of Natural Sciences, Amgueddfa Cymru – National Museum Wales, Cardiff,  
12 United Kingdom

13 <sup>5</sup>Department of Biological Sciences, University of Bergen, Bergen, Norway

14 <sup>6</sup>Institute of Zoology and Evolutionary Research, Friedrich-Schiller-University Jena, Jena,  
15 Germany

16 <sup>7</sup>Molecular Genetics Unit, Okinawa Institute of Science and Technology Graduate  
17 University, Okinawa, Japan

18 <sup>8</sup>Department of Genetics, Evolution and Environment, University College London, London,  
19 United Kingdom

20 § These authors contributed equally.

21 \* Correspondence: José M. Martín-Durán ([chema.martin@qmul.ac.uk](mailto:chema.martin@qmul.ac.uk)), Ferdinand Marlétaz  
22 ([f.marletaz@ucl.ac.uk](mailto:f.marletaz@ucl.ac.uk))

23

24 **Indirect development with an intermediate larva exists in all major animal lineages<sup>1</sup>,**  
25 **and thus larvae are central to most scenarios for animal evolution<sup>2-12</sup>. Yet how larvae**  
26 **evolved remains disputed. Here we show that changes in the timing of trunk formation**  
27 **underpin the diversification of larvae and bilaterian life cycles. Combining**  
28 **chromosome-scale genome sequencing with transcriptomic and epigenomic profiling in**  
29 **the slow-evolving oweniid *Owenia fusiformis*<sup>13</sup>, we found that different genes and**  
30 **genomic regulatory elements control the development of its feeding larva and adult**  
31 **stage. First, *O. fusiformis* embryos develop into an enlarged anterior domain that forms**  
32 **larval tissues and the adult head, as posterior growth and trunk patterning is deferred**  
33 **to pre-metamorphic stages. These traits also occur in the so-called “head larvae” of**  
34 **other bilaterians<sup>14,15</sup>, with whom *O. fusiformis* larva shows extensive transcriptomic**  
35 **similarities. Conversely, animals with non-feeding larvae and gradual metamorphoses,**  
36 **such as the annelid *Capitella teleta*, start trunk differentiation during embryogenesis,**  
37 **like direct developers. Together, our findings suggest that the ancestral temporal**  
38 **decoupling of head and trunk formation, as retained in extant “head larvae”, allowed**  
39 **larval evolution in Bilateria, questioning prevailing scenarios that propose either co-**  
40 **option<sup>10,11</sup> or innovation<sup>12</sup> of gene regulatory programmes to explain larva and adult**  
41 **origins.**

42

43 Many animal embryos develop into an intermediate, often free-living stage termed larva,  
44 which later metamorphoses into the sexually competent adult<sup>1,2</sup>. Larvae are vastly diverse and  
45 can display from radically different to more similar morphologies than those of their adults<sup>1,2</sup>.  
46 Given their broad phylogenetic distribution<sup>2</sup>, larvae are central to major scenarios of animal

47 evolution<sup>2-12</sup>. These fundamentally disagree on whether larvae are ancestral<sup>2-7</sup> or secondarily  
48 evolved<sup>10,11</sup> life stages and propose different mechanisms to explain the evolution of larva  
49 and adult forms (Fig. 1a, b). The “intercalation” hypothesis<sup>10,11</sup> suggests that larval stages  
50 were added to animal life cycles multiple times independently, by co-opting genes and  
51 genetic programmes originally expressed in the adult (Fig. 1a). Conversely, the “terminal  
52 addition” scenario<sup>2,3,12</sup> considers that the ancestral bilaterians resembled existing larvae, and  
53 thereby adults convergently evolved through the parallel evolution of adult-specific genetic  
54 programmes<sup>12</sup> (Fig. 1b). An assessment of the mechanisms underlying these hypotheses using  
55 comparative and functional genomics data is, however, lacking, and thus larval origins—and  
56 their importance to explain animal evolution—are still contentious.

57

58 The trochophore<sup>16</sup> is a widespread larval type generally characterised by an apical sensory  
59 organ and a pre-oral locomotive ciliary band<sup>17</sup> that is classically assigned to Annelida and  
60 Mollusca but also potentially to related clades within Lophotrochozoa<sup>18</sup> (Fig. 1c).

61 Trochophore larvae—traditionally exemplified by that of annelid worms—are pivotal to the  
62 “terminal addition” scenario<sup>2,19</sup>, which regards this larval type a vestige of the last common  
63 adult ancestor to Protostomia<sup>2,3</sup>, or even Bilateria<sup>20</sup> (Fig. 1c). Compared to most other annelid  
64 lineages, however, the larvae of the annelid groups Oweniidae and Magelonidae—which  
65 form Oweniida, the sister group to all other annelids<sup>13</sup>—exhibit unusual characters  
66 (Fig. 1c, d). In particular, the idiosyncratic oweniid larva, commonly referred to as  
67 “mitraria”<sup>21</sup>, has an enlarged pre-oral region and a single tuft of posterior chaetae, as well as a  
68 pair of nephridia and a long monociliated ciliary band alike those of phylogenetically distant  
69 larvae of deuterostome lineages, such as echinoderms and hemichordates<sup>22-24</sup>. Despite these  
70 distinctive larval traits, oweniids exhibit many developmental characters considered ancestral  
71 to Annelida, and even Lophotrochozoa as a whole<sup>25,26</sup>, as well as similarities in larval

72 molecular patterns with other trochophore and bilaterian larvae<sup>24,25,27,28</sup>. Consequently,  
73 whether the mitraria larva is the result of divergent or convergent evolution is unclear, which  
74 makes the comparative analysis of this lineage-restricted larva an excellent case study to  
75 investigate how larval traits evolve, and thereby formulate and assess scenarios on the origin  
76 of animal life cycles.

77

78 Here, we characterise the reference chromosome-scale genome assembly of the oweniid  
79 *Owenia fusiformis* (Fig. 1e) and perform a comprehensive study of its developmental  
80 transcriptome and regulatory genome that allows us to dissect the gene regulatory events  
81 underpinning the formation of the mitraria larva. The comparison of our comprehensive  
82 dataset with other lophotrochozoan and bilaterian taxa provides compelling evidence that  
83 heterochronic shifts in trunk development, rather than co-option and innovation in genetic  
84 programmes—as traditionally proposed—underpin the evolution of bilaterian life cycles.

85

## 86 **Results**

87 *O. fusiformis* has a conservatively evolving genome

88 To characterise the transcriptomic and genomic regulatory basis for larval development in  
89 *O. fusiformis*, we first generated a chromosome-scale reference assembly combining PacBio  
90 long-reads, 10x genomics read clouds, optical mapping, and Hi-C scaffolding (Extended Data  
91 Fig. 1a). Consistent with flow cytometry and *k*-mer estimations, the haploid assembly spans  
92 505.8 Mb (Extended Data Fig. 1b–d; Supplementary Fig. 1), exhibiting 12 chromosome-scale  
93 scaffolds that encompass 89.2% of the assembly (Extended Data Fig. 1e, f). Almost half of  
94 the assembly consists of repeats (43.02%; largely DNA transposons) acquired steadily during  
95 evolution (Extended Data Fig. 2a–c; Supplementary Table 1). Using transcriptomic data from

96 14 developmental stages and 9 adult tissues (Extended Data Fig. 1a), we annotated 26,966  
97 protein-coding genes and 31,903 transcripts, representing a nearly complete (97.5%) set of  
98 metazoan BUSCO genes (Extended Data Fig. 1g). Gene family reconstruction and principal  
99 component analysis on gene content across 22 animal genomes nested *O. fusiformis* within  
100 other non-annelid lophotrochozoan species (Fig. 1f), supporting that *O. fusiformis* has fewer  
101 gene family gains and losses, and retains more ancestral metazoan orthogroups than other  
102 annelid taxa (Fig. 1g; Extended Data Fig. 2d–i; Supplementary Tables 2–7). Therefore,  
103 *O. fusiformis* genome contains a more complete gene repertoire than those reported for other  
104 annelid lineages, which together with its phylogenetic position and conserved early  
105 embryogenesis<sup>25,26</sup> makes it a key lineage to reconstruct the evolution of Annelida and  
106 Lophotrochozoa generally.

107

108 Chromosomal linkage of orthologous genes between deuterostomes and protostomes supports  
109 the presence of 22 ancestral linkage groups in bilaterians<sup>29,30</sup>. To explore the conservation of  
110 the high-order organisation of *O. fusiformis* genome, we compared its syntenic orthology  
111 with the cephalochordate *Branchiostoma lanceolatum* (a deuterostome) and the mollusc  
112 *Pecten maximus* (a lophotrochozoan). *Owenia fusiformis* has globally retained the ancestral  
113 bilaterian linkage groups (Fig. 1h; Extended Data Fig. 2h, i) and exhibits chromosomal  
114 fusions that are present in the scallop and even a nemertean (H+Q, J2+L and K+O2), which  
115 are thus likely ancestral to Lophotrochozoa. While the nemertean *Lineus longissimus* presents  
116 only one more fusion in addition to these three ancestral lophotrochozoan chromosomal  
117 rearrangements, *O. fusiformis*, as well as the polychaete *Streblospio benedicti*, show  
118 additional fusions of ancestral bilaterian linkage groups, which are notably not shared  
119 between the two taxa and therefore none are ancestral to Annelida (Extended Data Fig. 2h, i).  
120 However, *O. fusiformis* still retains a more ancestral chromosomal organisation than

121 *S. benedicti*, in which all chromosomes except two are derived from secondary chromosomal  
122 fusion events, and other annelids with highly contiguous assemblies<sup>31,32</sup>. Together, our high-  
123 quality assembly of *O. fusiformis* supports that phylogenetically distant lophotrochozoan  
124 lineages largely share an ancestral syntenic chromosomal organisation, further revealing a  
125 dynamic chromosomal evolution in annelids, albeit their generally stable gene complement.

126

127 *O. fusiformis* larva does not co-opt genes expressed in the adult

128 The “intercalation” scenario proposes that larvae evolved secondarily by co-opting genes and  
129 gene modules expressed in adult stages<sup>10,11</sup> (Fig. 1a). Larva and adult would thus share  
130 transcriptional similarities, while more gradual transcriptional dynamics would be expected  
131 during direct development, as in the annelid *Dimorphilus gyrociliatus*<sup>31</sup>. To test this  
132 hypothesis, we used bulk stage-specific transcriptomic data from the blastula—the stage at  
133 which axial polarity is established in *O. fusiformis*<sup>26</sup>—to juvenile (as a proxy to adult stages),  
134 covering larval embryogenesis, growth, and metamorphosis (Fig. 2a; Extended Data Fig. 3a–  
135 f; Supplementary Tables 8–10). We observed two main phases of increased gene expression  
136 and differential gene expression activity during the life cycle of *O. fusiformis*, with the early  
137 mitraria as transitional stage: a first phase leading to larva formation (i.e., embryogenesis),  
138 followed by a second phase encompassing larval growth and metamorphosis into the juvenile  
139 (Fig. 2b, c; Extended Data Fig. 3g). Soft clustering and weighted gene co-expression network  
140 analysis of the 31,678 expressed transcripts generated an optimal number of 12 distinct  
141 clusters and 14 modules of temporally co-regulated genes, respectively, which broadly  
142 classified as peaking during either the first or the second transcriptional phases (Extended  
143 Data Fig. 4; Supplementary Fig. 2–4; Supplementary Tables 11–13). In none of the two  
144 approaches, however, were there clusters of genes with peaks of expression at both the



145 mitraria and the juvenile stage, and only one cluster (1,426 transcripts; 4.5%) showed a  
146 bimodal activation at blastula and juvenile stages (Extended Data Fig. 4a). Therefore,  
147 extensive co-option of adult genes into larva embryogenesis—as the “intercalation” scenario  
148 posits—does not occur in *O. fusiformis*, and instead larval embryogenesis and juvenile/adult  
149 development are two markedly distinct transcriptional phases.

150

151 *Trunk development is delayed to pre-metamorphosis in O. fusiformis*

152 To identify the developmental processes underpinning the two transcriptional phases during  
153 *O. fusiformis* life cycle, we performed gene ontology (GO) enrichment analyses on the soft  
154 clusters and modules of temporally co-regulated genes (Extended Data Fig. 4b–l). GO terms  
155 related to nucleic acid metabolism—i.e., DNA replication and transcription—and complex  
156 biosynthetic metabolism predominate in clusters of the first transcriptional phase (Extended  
157 Data Fig. 4b–f), consistent with the establishment of the larval body plan and development of  
158 the functional digestive system at those stages<sup>21,25</sup>. Among the genes expressed in this first  
159 phase, we identified an ortholog of *chordin*, a key bone morphogenetic protein (BMP)  
160 inhibitor involved in dorsoventral patterning across Bilateria<sup>33</sup> and thought to be lost in  
161 annelids<sup>34</sup> (Fig. 2d; Extended Data Fig. 5a, b). With a complex pattern of retentions and  
162 losses in Annelida (Extended Data Fig. 5c–f; Supplementary Tables 14–18), *chordin* is  
163 asymmetrically localised around the blastopore lip of the gastrula and later in the larval  
164 antero-ventral oral ectoderm (Fig. 2e). This expression resembles that of molluscs<sup>34,35</sup> and  
165 brachiopods<sup>28</sup>, providing further evidence that conserved developmental mechanisms  
166 underpin larval formation in *O. fusiformis*<sup>26-28</sup>. However, differently from non-feeding  
167 annelid trochophores<sup>6</sup>, anterior ectodermal genes<sup>26-28</sup> pattern most larval tissues in

168 *O. fusiformis* (Fig. 2f), whereas posterior genes are restricted to few circum-anal cells, in line  
169 with the vastly enlarged pre-oral region of the mitraria that forms early on in the adult head<sup>21</sup>.  
170

171 GO terms involved in terminal cell differentiation, morphogenesis, and organogenesis  
172 predominate in co-expression clusters of the second transcriptional phase. *Hox* genes, a  
173 conserved family of transcription factors involved in anterior-posterior trunk regionalisation  
174 in Bilateria<sup>36</sup>, are among the most upregulated genes at these stages (Fig. 2g).

175 *Owenia fusiformis* has a conserved complement of 11 *Hox* orthologues arranged as a  
176 compact, ordered cluster in chromosome 1, except for *Post1*, which is located downstream on  
177 that same chromosome (Extended Data Fig. 6a–c; Supplementary Table 19). This is a similar  
178 repertoire and genomic arrangement to that of the annelids *Capitella teleta*<sup>37</sup> and  
179 *Platynereis dumerilii*<sup>38</sup>; yet unlike these annelids, which deploy *Hox* genes during or soon  
180 after gastrulation<sup>37,39</sup> (Extended Data Fig. 6d), *O. fusiformis* does not express *Hox* genes  
181 during embryogenesis to pattern the larval body (Fig. 2h; Extended Data Fig. 6d, e). Instead,  
182 *Hox* genes are expressed in the trunk rudiment during larval growth, already in an anterior–  
183 posterior staggered pattern that is retained in the juvenile after metamorphosis (Fig. 2h–j;  
184 Extended Data Fig. 6e). This late activation of *Hox* genes is not unique to *O. fusiformis* but  
185 also occurs in the planktotrophic trochophore of the echiuran annelid *Urechis unicinctus*  
186 (Extended Data Fig. 6d; Supplementary Table 20). Therefore, posterior/trunk development is  
187 deferred to pre-metamorphic stages in planktotrophic annelid trochophores<sup>14,40</sup> compared to  
188 annelids with lecithotrophic larvae<sup>37,38</sup> and direct developers<sup>31</sup> (Extended Data Fig. 6f).

189 Altogether, our findings support that axial and body patterning, as well as anterior and gut  
190 differentiation contribute to the first transcriptional phase, while adult trunk formation largely  
191 drives the second post-embryonic transcriptional phase during *O. fusiformis* life cycle.

192

193 *Chromatin dynamics support two regulatory modules during Owenia development*

194 To investigate the genomic regulatory basis for the observed temporal decoupling of head  
195 and trunk development in *O. fusiformis*, we profiled open chromatin regions with ATAC-seq  
196 at five developmental stages, from blastula to competent larva (Fig. 2a; Extended Data  
197 Fig. 7a–e, Supplementary Tables 21–24). In total, we identified 47,406 consensus regulatory  
198 regions (Extended Data Fig. 7f, g), mostly abundant within gene bodies (68.14%) rather than  
199 in promoters (16.19%) and distal intergenic regions (15.67%) (Fig. 3a, Supplementary  
200 Table 23). While the total number of accessible regions is greater during embryogenesis than  
201 in larval stages (Fig. 3b; Extended Data Fig. 7f–h), the largest changes in peak accessibility  
202 occur in the mitraria and competent larva (Fig. 3c, Supplementary Table 24). At these stages,  
203 there is an increase in ATAC-seq peak width and proportion of accessible chromatin in  
204 promoters and upstream gene body elements (i.e., 5' UTRs and first exons; Extended Data  
205 Fig. 7i, j; Extended Data Fig. 8a), which are regulatory regions that correlate positively with  
206 gene expression (Extended Data Fig. 8b). Soft clustering revealed that most regulatory  
207 regions act during either embryogenesis (29,611; 63.99%) or larval growth (13,457; 29.08%),  
208 with just 3,210 peaks (6.93%; cluster 8) being accessible from gastrula to mitraria (Fig. 3d).  
209 To explore the interplay between regulatory and transcriptional programmes, we predicted *de*  
210 *novo* DNA binding motifs on ATAC-seq peaks located in promoters and intergenic regions.  
211 Soft clustering in six optimal groups according to their differential use during *O. fusiformis*  
212 life cycle recovered two main regulatory modules, one mostly active during embryogenesis  
213 and a second mostly used during larval growth (Fig. 3e; Extended Data Fig. 8c–e,  
214 Supplementary Tables 25, 26, Supplementary Fig. 5, 6). Consistent with our transcriptomic  
215 dataset, motifs related to transcription factors involved in patterning anterior territories (e.g.,  
216 PAX2/5/8 and PAX4/6<sup>27</sup>), muscle and gut development (GATA<sup>28</sup>, FOXC<sup>28</sup>) and early

217 neurogenesis (ATOH<sup>41</sup>) are amongst the most differentially accessible in open chromatin  
218 regions during embryogenesis, whilst ciliary band genes (OTX<sup>28</sup>), trunk related genes (e.g.,  
219 NKX2.1<sup>27</sup>) and most notably *Hox* genes appear in regulatory regions during larval  
220 competence and trunk patterning (Fig. 3e; Extended Data Fig. 8c). Therefore, two different  
221 sets of *cis*-regulatory elements mirror the major transcriptional dynamics in *O. fusiformis*,  
222 reinforcing the view that separate genetic mechanisms that are temporally decoupled  
223 underpin larva and adult formation in this annelid.

224

#### 225 *Mitraria development does not rely on novel genes*

226 Novel genes account for a significant proportion of some trochophore and other larval  
227 transcriptomes<sup>7,42</sup>, as they might be associated with the development of larval-specific  
228 characters (e.g., ciliary bands)<sup>7,42,43</sup>. Therefore, recruitment of novel genes at the mitraria  
229 stage could also explain the overall transcriptomic differences between this and the adult  
230 stage, as well as the distinctive morphological traits of this larval form. To define the  
231 contribution of novel genes at each developmental stage in *O. fusiformis*, we classified all  
232 predicted transcripts in seven phylostrata according to their time of origin (Fig. 4a,  
233 Supplementary Table 27). Older genes (genes of metazoan and pre-metazoan origin;  
234 phylostratum 1) represent the largest fraction of genes expressed at all developmental stages  
235 except that of the juvenile in *O. fusiformis*, whereas the highest expression levels of  
236 novel/younger genes (phylostratum 7) occur in the juvenile stage (Fig. 4b, Extended Data  
237 Fig. 9a–d). An enrichment analysis of each phylostrata on each of the 12 recovered gene  
238 cluster showed that older genes are significantly enriched in early embryonic stages (clusters  
239 1 to 3), while novel genes are significantly overrepresented in gene clusters active at the  
240 juvenile stage and most notably, underrepresented in the mitraria larva (clusters 7 and 8;

241 Extended Data Fig. 9e). Therefore, older rather than younger genes contribute to the  
242 development of the mitraria larva, suggesting that the increased use of novel genes in other  
243 lophotrochozoan larvae<sup>7,42</sup> might be due to lineage-specific traits found on those larvae, such  
244 as the shell primordium of molluscan trochophores<sup>7</sup> and perhaps even ciliary bands with  
245 multiciliated cells<sup>44</sup>, which are absent in oweniid larvae.

246

#### 247 *Bilaterian planktotrophic larvae share maximal transcriptional similarity*

248 The “terminal addition” scenario<sup>2,3,19</sup> posits that larvae are homologous and adults evolved  
249 convergently, and thus pre-larval stages should be more conserved than metamorphosis and  
250 adult stages across species<sup>11</sup> (Fig. 1b). To test this hypothesis, we first generated bulk stage-  
251 specific transcriptomic data for the annelid *C. teleta* (Supplementary Fig. 7, Supplementary  
252 Table 28), which exhibits a typical lecithotrophic trochophore (Fig. 1c). Differently from  
253 *O. fusiformis*, *C. teleta* does not show two marked transcriptional phases but rather a gradual  
254 increase of gene expression during its life cycle (Fig. 4c), as direct developers do<sup>31</sup>. Pairwise  
255 transcriptomic comparisons between *O. fusiformis* and *C. teleta* demonstrate overall similar  
256 transcriptional dynamics between the development of these annelids, yet the point of  
257 maximal transcriptional divergence occurs at larval—and not adult—stages (Fig. 4d). While  
258 this observation disagrees with the “terminal addition” scenario, it rather reflects, and is  
259 explained by, the different timings of trunk differentiation in *O. fusiformis* and *C. teleta*  
260 (Extended Data Fig. 6f).

261

262 We thus extended our comparative transcriptomic approach to six other bilaterian lineages  
263 and the cnidarian *Nematostella vectensis* to cover the overall diversity of life cycle strategies  
264 found in Metazoa, using both all single copy one-to-one orthologs (Fig. 4a, e; Extended Data

265 Fig. 10a; Supplementary Tables 29, 30) and a reduced set of conserved cross-species single  
266 copy orthologs (Extended Data Fig. 10b, c). Transcriptional dynamics between *O. fusiformis*  
267 and other major animal groups are more dissimilar (except in *Danio rerio*) at early  
268 development and become more similar as development proceeds towards juvenile and adult  
269 stages (Fig. 4e, f; Extended Data Fig. 10a–c; Supplementary Tables 31, 32). At the larval  
270 stage, *O. fusiformis* shows vast transcriptomic differences with the larvae of *Drosophila*  
271 *melanogaster* and *Caenorhabditis elegans*, the two ecdysozoan taxa with indirect  
272 development and whose larvae evolved secondarily<sup>10</sup> (Fig. 4f). However, *O. fusiformis* shares  
273 maximal transcriptomic similarities at larval stages with bilaterian species with  
274 planktotrophic ciliated larvae and even the early planula of the cnidarian *Nematostella*  
275 *vectensis* (Fig. 4e, f; Extended Data Fig. 10a, b). Together, these findings question the  
276 “terminal addition” scenario, because adult development is generally more conserved than  
277 embryogenesis, but also reveal unexpected genome-wide transcriptional similarities between  
278 phylogenetically distant bilaterian planktotrophic larvae.

279

## 280 **Discussion**

281 In this study, we report the chromosome-scale genome assembly of the oweniid *O. fusiformis*  
282 which, together with extensive gene expression and genomic regulatory profiling during  
283 embryonic and larval development, provides an unprecedented perspective on mainstream  
284 scenarios for life cycle evolution in Bilateria. In particular, our results refute predictions that  
285 propose either the co-option of adult genes into larval gene regulatory programmes<sup>10,11</sup> (in  
286 line with the “intercalation” scenario) or the independent evolution of adult gene regulatory  
287 modules<sup>2,3,19</sup> (as it would be expected in the “terminal addition” scenario) as drivers of larva  
288 and adult evolution, respectively. Instead, the distinctive mitraria larva of *O. fusiformis*

289 develops from an enlarged head region while trunk differentiation is deferred to late larval  
290 stages (Fig. 5a; Extended Data Fig. 6f). Similar developmental traits occur in other feeding  
291 annelid larvae<sup>40</sup> (Extended Data Fig. 6e) including that of *Chaetopterus*<sup>45,46</sup>, a member of the  
292 second earliest branching annelid lineage<sup>47</sup>, as well as in other phylogenetically distant clades  
293 within Lophotrochozoa (e.g., nemerteans<sup>48</sup> and phoronids<sup>49</sup>), Ecdysozoa (pancrustaceans<sup>15</sup>  
294 and pycnogonids<sup>50</sup>), and Deuterostomia (e.g., echinoderms<sup>51,52</sup> and hemichordates<sup>53</sup>), whose  
295 larvae are generally referred to as “head larvae”<sup>14,15</sup>. By contrast, non-feeding larvae<sup>37,39</sup> and  
296 direct developers<sup>31</sup> in both Annelida (Extended Data Fig. 6f) and other bilaterian taxa<sup>54,55</sup>  
297 start trunk patterning soon after gastrulation (Fig. 5b), while the onset of anterior/head  
298 patterning always takes place before gastrulation in bilaterians<sup>56</sup>. Regardless of these different  
299 timings, major bilaterian clades share head<sup>57,58</sup> and trunk molecular patterns (e.g., a *Hox*  
300 code<sup>36</sup>; Fig. 2h), supporting the overall homology of the adult bilaterian body plan. Therefore,  
301 our findings indicate that heterochronic shifts of an adult trunk developmental programme  
302 correlate with, and may account for, the evolution of the different life cycles in Annelida, and  
303 Bilateria generally<sup>53</sup>.

304

305 The post-embryonic activation of genetic programmes involved in trunk differentiation  
306 observed in “head larvae” has generally been considered a lineage-specific innovation  
307 associated with the evolution of maximal indirect development<sup>14,15,23,49</sup>. Consequently, “head  
308 larvae” are thought to have evolved convergently and the observed similarities in larval  
309 molecular patterns<sup>6,49,53,59</sup> might reflect ancient gene regulatory modules that were  
310 independently co-opted to develop analogous larval organs (e.g., apical organs and ciliary  
311 bands), in line with the “intercalation” scenario<sup>10,11</sup>. In contrast, our study supports that the  
312 late deployment of trunk differentiation programmes is likely ancestral to Annelida (Fig. 5c),  
313 and not necessarily related to maximal indirect development. Indeed, an ancestral post-

314 embryonic onset of trunk differentiation is a more parsimonious state for Bilateria, based on  
315 our current understanding of the timing of trunk-associated expression of *Hox* genes in major  
316 bilaterian clades and cnidaria (Extended Data Fig. 10d; Supplementary Table 33). This  
317 temporal decoupling between head and trunk genetic programmes could thus have facilitated  
318 the evolution of larvae, which would then be homologous on the grounds of being largely  
319 anteriorly derived transitory structures that form intermediate life cycle specialisations.  
320 Notably, this scenario does not exclude the possibility that as bilaterians (and thus larvae)  
321 diversified, conserved gene regulatory modules were also convergently reused to develop  
322 analogous larval organs in different lineages. Regardless of the scenario, however, our study  
323 highlights the importance of heterochronic changes in the deployment of ancient genetic  
324 programmes for the diversification of bilaterian life cycles, which had profound ecological  
325 and evolutionary implications. In the future, comparative genomic studies that thoroughly  
326 dissect the regulatory principles underlying head and trunk development in multiple bilaterian  
327 lineages will help to decipher how temporal changes in their deployment drove the evolution  
328 of larval and adult forms in Bilateria.

329

## 330 **Materials and Methods**

### 331 *Adult culture, spawning and in vitro fertilisation*

332 Sexually mature *Owenia fusiformis* Delle Chiaje, 1844 adults were collected from subtidal  
333 waters near the Station Biologique de Roscoff and cultured in the lab as described before<sup>25</sup>. *In*  
334 *vitro* fertilisations and collections of embryonic and larval stages were performed as  
335 previously described<sup>25</sup>. *Capitella teleta* Blake, Grassle & Eckelbarger, 2009 was cultured,  
336 grown, and sifted, and its embryos and larvae were collected following established  
337 protocols<sup>60</sup>. *Magelona* spp. were collected in muddy sand from the intertidal of Berwick-



338 upon-Tweed, Northumberland, NE England (~55.766781, -1.984587) and kept initially in  
339 aquaria at the National Museum Cardiff before their transfer to Queen Mary University of  
340 London, where they were kept in aquaria with artificial sea water.

341

#### 342 *Genome size measurements*

343 To estimate the haploid DNA nuclear content of *O. fusiformis*, we used a flow cytometer  
344 Partex CyFlow Space fitted with a Cobalt Samba green laser (532 nm, 100 mW) as described  
345 for the annelid *Dimorphilus gyrociliatus*<sup>25</sup> and adult individuals of *Drosophila melanogaster*  
346 as reference. Additionally, we used Jellyfish v.2.3<sup>61</sup> to count and generate a 31-mer histogram  
347 from adaptor-cleaned, short-read Illumina reads (see section below), and GenomeScope 2.0<sup>62</sup>  
348 to obtain an in-silico estimation of the genome size and heterozygosity of *O. fusiformis*.

349

#### 350 *Genome sequencing, assembly, and quality check*

351 Ultra-high molecular weight (UHMW) genomic DNA (gDNA) was extracted following the  
352 Bionano genomics IrysPrep agar-based, animal tissue protocol using sperm from a single *O.*  
353 *fusiformis* male. UHMW gDNA was cleaned up using a salt:chloroform wash following  
354 PacBio's recommendations before long-read sequencing using PacBio v3.0 chemistry at the  
355 University of California Berkeley. A total of 16 SMRT cells of PacBio Sequel were used for  
356 sequencing with 600 min movie time, producing a total of 170.07 Gb of data (10.72 million  
357 reads, N50 read length between 25.75 kb and 30.75 kb). In addition, we used UHMW gDNA  
358 of that same individual to generate a 10x Genomics linked reads library, which we sequenced  
359 in an Illumina HiSeq4000 at Okinawa Institute of Science and Technology (OIST) to produce  
360 28.62 Gb of data (141.66 million read pairs). PacBio reads were assembled with CANU  
361 v.8.3rc2<sup>63</sup> assuming 'batOptions="-dg 3 -db 3 -dr 1 -ca 500 -cp 50' and

362 ‘correctedErrorRate=0.065’. Pacbio reads were remapped using pbalign v.0.3.2 and the  
363 assembly polished once using Arrow (genomicconsensus, v2.3.2). Then Illumina paired end  
364 reads generated with the 10x Genomics linked reads were extracted, remapped using bwa  
365 mem v.0.7.17<sup>64</sup> and used for polishing with Racon v.1.16<sup>65</sup>. Bionano Genomics optical  
366 mapping data was used to scaffold the PacBio-based assembly, which was de-haploidised  
367 with purge\_haplotigs v.1.0.4<sup>66</sup> setting cut-offs at 35, 85 and 70x coverages to reconstruct a  
368 high-quality haploid reference assembly. HiC-based chromosome scaffolding was performed  
369 as described below. Merqury v.1.1<sup>67</sup> and BUSCO v.5<sup>68</sup> were used to assess genome  
370 completeness and evaluate the quality of the assembly.

371

### 372 *Transcriptome sequencing*

373 Fourteen samples spanning key developmental time points of *O. fusiformis* life cycle,  
374 including active oocyte, zygote, 2-cell, 4-cell, and 8-cell stages, 3 hours post-fertilisation  
375 (hpf), 4 hpf, coeloblastula (5 hpf), gastrula (9 hpf), axial elongation (13 hpf), early larva  
376 (18 hpf), mitraria larva (27 hpf), pre-metamorphic competent larva (3 weeks post-  
377 fertilisation, wpf) and post-metamorphic juvenile were collected in duplicates (except for the  
378 latter), flash frozen in liquid nitrogen and stored at -80 °C for total RNA extraction. Samples  
379 within replicates were paired, with each one containing ~300 embryos or ~150 larvae coming  
380 from the same *in vitro* fertilisation. Nine further samples from adult tissues and body regions  
381 (blood vessel, body wall, midgut, prostomium, head, ovary, retractor muscle, tail, and testes)  
382 were also collected as described above. Likewise, further five samples spanning post-  
383 cleavage time points of *C. teleta*, including 64-cell stage, gastrula, stage 4tt, stage 5, and  
384 stage 7 larva, were also collected in duplicates. Total RNA was isolated with the Monarch  
385 Total RNA Miniprep Kit (New England Biolabs, NEB) following supplier’s

386 recommendations. Total RNA samples from developmental stages from both *O. fusiformis*  
387 and *C. teleta* were used to prep strand-specific mRNA Illumina libraries that were sequenced  
388 at the Oxford Genomics Centre (University of Oxford, UK) over three lanes of an Illumina  
389 NovaSeq6000 system in  $2 \times 150$  bases mode. Adult tissue samples were sequenced at BGI on  
390 a BGISEq-500 platform in  $2 \times 100$  bases mode. All samples were sequenced to a depth of  
391 ~50 M reads (Supplementary Tables 8, 28).

392

### 393 *Annotation of repeats and transposable elements (TEs)*

394 RepeatModeler v.2.0.1<sup>69</sup> and RepBase were used to construct a *de novo* repeat library for  
395 *O. fusiformis*, which was then filtered for *bona fide* genes using the predicted proteome of *C.*  
396 *teleta* available at Ensembl Metazoa as reference. The filtered consensus repeat predictions  
397 were then used to annotate the genome assembly of *O. fusiformis* with RepeatMasker “open-  
398 4.0”. We next used LTR\_finder v.1.07<sup>70</sup>, a structural search algorithm, to identify and  
399 annotate Long Tandem Repeats (LTR). Finally, we generated a consensus set of repeats by  
400 merging RepeatMasker and LTR\_finder predictions with RepeatCraft<sup>71</sup>, using default  
401 parameters but a maximum LTR size of 25 kb (as derived from the LTR\_finder annotation).  
402 The general feature format (gff) file with the annotation of TEs and repeats is in *O. fusiformis*  
403 genome repository (see Data Availability section).

404

### 405 *Gene prediction and functional annotation*

406 We used SAMtools v.1.9<sup>72</sup> and the annotation of repeats to soft-mask *O. fusiformis* genome  
407 assembly before gene prediction. We then mapped all embryonic and adult transcriptomes  
408 and a publicly available dataset<sup>47</sup> (SRR1222288) with STAR v. 2.5.3a<sup>73</sup> after removing low-  
409 quality read pairs and read pairs containing Illumina sequencing adapters with trimmomatic

410 v.0.39<sup>74</sup>. StringTie v.1.3.6<sup>75</sup> was used to convert STAR alignments into gene transfer format  
411 (GTF) files and Portcullis v.1.1.2<sup>76</sup> to generate a curated set of splice junctions. Additionally,  
412 we generated *de novo* transcriptome assemblies for all samples with Trinity v.2.5.1<sup>77</sup> with  
413 default parameters, which were thereafter mapped to the soft-masked assembly with GMAP  
414 v.2020-04-08<sup>78</sup>. We then ran the default Mikado v.2.1 pipeline<sup>79</sup> to merge all transcriptomic  
415 evidence and reliable splice junctions into a single set of best-supported transcripts and gene  
416 models. From this merged dataset, we filtered full-length, non-redundant transcripts with a  
417 BLAST hit on at least 50 % of their length and at least two exons to obtain a gene set that we  
418 used to train Augustus v.3.2.3<sup>80</sup>. Simultaneously, we used the Mikado gene annotation and  
419 Portcullis splice junctions to generate confident sets of exon and intron hints, respectively.  
420 We also ran Exonerate v.2.4.0<sup>81</sup> to generate spliced alignments of the proteome of *C. teleta*  
421 proteome on *O. fusiformis* soft-masked genome assembly to obtain further gene hints. We  
422 then merged all exon and intron hints into a single dataset which we passed to Augustus  
423 v.3.2.3<sup>80</sup> for *ab initio* gene prediction. Finally, PASA v.2.3.3<sup>82</sup> was used to combine RNA-seq  
424 and *ab initio* gene models into a final gene set, from which spurious predictions with in-frame  
425 STOP codons (228 gene models), predictions that overlapped with repeats (5,779 gene  
426 models) and that had high similarity to transposable elements in the RepeatPeps.lib database  
427 (2,450 models) were removed. This filtered gene set includes 26,966 genes, encompassing  
428 31,903 different transcripts. To assess the completeness of this annotation, we ran BUSCO  
429 v.5<sup>68</sup> in proteome mode, resulting in 97.7 % of the core genes present. Protein homologies for  
430 the 34,353 filtered transcripts were annotated with BLAST v.2.2.31+<sup>83</sup> on the  
431 UniProt/SwissProt database provided with Trinotate v.3.0<sup>84</sup>. We used HMMER v.2.3.2<sup>85</sup> to  
432 identify protein domains using Trinotate's PFAM-A database and signalP v.4.1<sup>86</sup> to predict  
433 signal peptides. These functional annotations were integrated into a Trinotate database, which  
434 retrieved Gene Ontology (GO), eggNOG and KEGG terms for each transcript. In addition,

435 we ran PANTHER HMM scoring tool to assign a PantherDB<sup>87</sup> orthology ID to each  
436 transcript. In total, we retrieved a functional annotation for 22,516 transcripts (63.86 %). The  
437 functional annotation report is provided in *O. fusiformis* genome repository (see Data  
438 Availability section).

439

#### 440 *Chromosome-scale scaffolding*

441 Sperm from a single *O. fusiformis* worm and an entire sexually mature male were used as  
442 input material to construct two Omni-C Dovetail libraries following manufacturer's  
443 recommendations for marine invertebrates. These libraries were sequenced in an Illumina  
444 NovaSeq6000 at the Okinawa Institute of Science and Technology (Okinawa, Japan) to a  
445 depth of 229 and 247 million reads. HiC reads were processed using the Juicer pipeline  
446 r.e0d1bb7<sup>88</sup> to generate a list of curated contracts ('merged no dups') that was subsequently  
447 employed to scaffold the assembly using 3d-dna v.180419<sup>89</sup>. The resulting assembly and  
448 contact map was visually inspected and curated using Juicebox v.1.11.08<sup>88</sup> and adjustments  
449 submitted for a subsequent run of optimisation using 3d-dna. Finally, repeats and TEs were  
450 re-annotated in this chromosome scale assembly as described above, and the annotation  
451 obtained for the PacBio-based assembly was lifted over with Liftoff v.1.6.1<sup>90</sup>. All gene  
452 models but two were successfully re-annotated in the chromosome-scale assembly.

453

#### 454 *Gene family evolution analyses*

455 We used the AGAT suite of scripts to generate non-redundant proteomes with only the  
456 longest isoform for a set of 21 metazoan proteomes (Supplementary Table 2). To reconstruct  
457 gene families, we used OrthoFinder v.2.2.7<sup>91</sup> using MMSeqs2<sup>92</sup> to calculate sequence  
458 similarity scores and an inflation value of 2. OrthoFinder gene families were parsed and

459 mapped onto a reference species phylogeny to infer gene family gains and losses at different  
460 nodes and tips using the ETE 3 library<sup>93</sup>, as well as to estimate the node of origin for each  
461 gene family. Gene expansions were computed for each species using a hypergeometric test  
462 against the median gene number per species for a given family employing previously  
463 published code<sup>31</sup>. Principal component analysis was performed on the orthogroups matrix by  
464 metazoan lineage, given that orthogroups were present in at least three of the 22 analysed  
465 species, to eliminate taxonomically restricted genes.

466

#### 467 *Macrosynteny analyses*

468 Single copy orthologues obtained using the mutual best hit (MBH) approach generated using  
469 MMseqs2<sup>92</sup> using the annotations of *Branchiostoma floridae*<sup>94</sup>, *Pecten maximus*<sup>95</sup>,  
470 *Streblospio benedictii*<sup>96</sup>, and *Lineus longissimus*<sup>97,98</sup> were used to generate Oxford synteny  
471 plots comparing sequentially indexed orthologue positions. Plotting order was determined by  
472 hierarchical clustering of the shared orthologue content using the complete linkage method as  
473 originally proposed. Comparison of the karyotype of all four species was performed using the  
474 Rideogram package by colouring pairwise orthologues according to the ALG assignment in  
475 comparisons with *P. maximus* and *B. floridae*.

476

#### 477 *Gene expression profiling*

478 To profile gene expression dynamics from blastula to juvenile stages (*O. fusiformis*) and from  
479 64-cell to competent larva stages (*C. teleta*), sequencing adaptors were removed from raw  
480 reads using trimmomatic v.0.39<sup>74</sup>. Cleaned reads were pseudo-aligned to the filtered gene  
481 models using kallisto v.0.46.2<sup>99</sup> (Supplementary Table 9) and genes with an expression level  
482 above an empirically defined threshold of 2 transcripts per million (TPM) were deemed

483 expressed (Extended Data Fig. 3f). DESeq2 v.1.30.1 package<sup>100</sup> was used to normalise read  
484 counts across developmental stages (Supplementary Table 10) and to perform pair-wise  
485 differential gene expression analyses between consecutive stages. *P*-values were adjusted  
486 using the Benjamini-Hochberg method for multiple testing correction. We defined a gene as  
487 significantly upregulated for a  $\log_2(\text{fold-change})$  (LFC) > 1 or downregulated for a LFC < 1,  
488 given that adjusted *p*-value < 0.05 (Supplementary Information). Principal component  
489 analysis was performed on a variance stabilising-transformed matrix of the normalised  
490 DESeq2 matrix. *Hox* gene expression profiling in *Urechis unicinctus*, was performed as  
491 described for *O. fusiformis* gene profiling, using an available reference transcriptome<sup>101</sup>.

492

#### 493 *Gene clustering and co-expression network analyses*

494 Genes were clustered according to their normalised expression dynamics through soft *k*-  
495 means clustering using the mfuzz v.2.52 package<sup>102</sup>. From all 31,903 genes, we discarded 225  
496 genes which were not expressed at any stage. We then determined an optimal number of 12  
497 clusters for our dataset by applying the elbow method to the minimum centroid distance as a  
498 function of the number of clusters. For the construction of the gene co-expression network,  
499 we used the WGCNA package v.1.70–3<sup>103</sup>. All 31,678 genes expressed at any developmental  
500 stage were used to build a signed network with a minimum module size of 300 genes and an  
501 optimised soft-thresholding power of 16. Block-wise network construction returned 15 gene  
502 modules, from which one module was dropped due to poor intramodular connectivity. The  
503 remaining 14 gene modules (A–N) were labelled with distinct colours with unassigned genes  
504 labelled in grey. A random subset consisting of the nodes and edges of 30 % of the genes was  
505 fed to Cytoscape v.3.8.2<sup>104</sup> for network visualisation. Module eigengenes were chosen to  
506 summarise the gene expression profiles of gene modules. Gene ontology (GO) enrichment

507 analyses of each gene cluster and gene module were performed using the topGO v.2.44  
508 package. We performed a Fisher's exact test and listed the top 30 (soft *k*-means clustering) or  
509 top 15 (WGCNA modules) significantly enriched GO terms of the class Biological Process.  
510 To ease visualisation, all 288 non-redundant enriched GO terms from all 12 gene clusters  
511 were clustered through *k*-means by semantic similarity using the simplifyEnrichment v.1.2.0  
512 package<sup>105</sup> (Supplementary Fig. 3).

513

#### 514 *Gene orthology assignment*

515 The identification of *chordin* (*chrd*), *chordin-like* (*chrld*) and *Hox* genes in *O. fusiformis* was  
516 based on the genome functional annotation. To mine *chrd* orthologues, 81 annelid  
517 transcriptomic datasets were downloaded from SRA (Supplementary Table 14) and  
518 assembled with Trinity v.2.5.1<sup>77</sup> to create BLAST local nucleotide databases. We also created  
519 a nucleotide database for *C. teleta* using its annotated genome<sup>29</sup> (ENA accession number  
520 GCA\_000328365.1). Human and *O. fusiformis* CHRDL proteins were used as queries to find  
521 *chrd* orthologues following the MBH approach ( $e\text{-value} \leq 10^{-3}$ ), obtaining 104 unique  
522 candidate *chrd* transcripts that were then translated (Supplementary Table 15). A single  
523 candidate CHRDL protein for *Themiste lageniformis* (unpublished data, provided by Michael J  
524 Boyle) was included *ad hoc* at this step. In addition, 15 curated CHRDL and CHRDL protein  
525 sequences (and an outgroup) were fetched from various sources (Supplementary Table 16)  
526 and aligned together with *O. fusiformis* CHRDL and CHRDL sequences in MAFFT v.7<sup>106</sup> with  
527 the G-INS-I iterative refinement method and default scoring parameters. From this mother  
528 alignment further daughter alignments were obtained using “mafft --addfragments”<sup>107</sup>, the  
529 accurate “--multipair” method, and default scoring parameters. For orthology assignment,  
530 two phylogenetic analyses were performed on selected candidate sequences, which included



531 the longest isoform for each species-gene combination, given that it included a 10-residue or  
532 longer properly aligned fragment in either the CHR domains or the von Willebrand factor  
533 type C (VWFC) domains (Extended Data Figure 5c, d). vWFC and CHR domains were  
534 trimmed and concatenated using domain boundaries defined by ProSITE domain annotation  
535 for the human chordin precursor protein (UniProt: Q9H2X0). Either all domains or the  
536 VWFC domains only were used for phylogenetic inference with a WAG amino acid  
537 replacement matrix<sup>108</sup> to account for transition rates, the FreeRate heterogeneity model  
538 (R4)<sup>109</sup> to describe sites evolution rates, and an optimization of amino acid frequencies using  
539 maximum likelihood (ML) using IQ-TREE v.2.0.3<sup>110</sup>. 1,000 ultrafast bootstraps (BS)<sup>111</sup> were  
540 used to extract branch support values. Bayesian reconstruction in MrBayes v.3.2.7a<sup>112</sup> were  
541 also performed using the same WAG matrix but substituting the R4 model for the discrete  
542 gamma model<sup>113</sup>, with 4 rate categories (G4). For the orthology assignment of *Hox* genes,  
543 129 curated *Hox* sequences were retrieved from various databases (Supplementary Table 19)  
544 and aligned with *O. fusiformis* *Hox* proteins with MAFFT v.7 in automatic mode. Poorly  
545 aligned regions were removed with gBlocks v.0.91b<sup>114</sup> yielding the final alignments.  
546 Maximum likelihood trees were constructed using RAxML v.8.2.11.9<sup>115</sup> with an LG  
547 substitution matrix<sup>116</sup> and 1,000 ultrafast BS. All trees were composed in FigTree v.1.4.4.  
548 Alignment files are available in *O. fusiformis* genome repository (see Data Availability  
549 section).

550

#### 551 *Whole mount in situ hybridisation and immunohistochemistry*

552 Fragments of *chordin* and *Hox* genes were isolated as previously described<sup>26</sup> using gene-  
553 specific oligonucleotides and a T7 adaptor. Riboprobes were synthesise with the T7  
554 MEGAscript kit (ThermoFisher, AM1334) and stored at a concentration of 50 ng/μl in

555 hybridisation buffer at  $-20^{\circ}\text{C}$ . Whole mount *in situ* hybridisation in embryonic, larval, and  
556 juvenile stages were conducted as described elsewhere<sup>26,28</sup>. Antibody staining in larval stages  
557 of *O. fusiformis*, *Magelona* spp. and *C. teleta* was carried out as previously described<sup>25,117</sup>.  
558 DIC images of the colorimetric *in situs* were obtained with a Leica 560 DMRA2 upright  
559 microscope equipped with an Infinity5 camera (Lumenera). Fluorescently stained samples  
560 were scanned with a Nikon CSU-W1 Spinning Disk Confocal.

561

#### 562 *Assay for Transposase-Accessible Chromatin using sequencing (ATAC-seq)*

563 We performed two replicates of ATAC-seq from samples containing  $\sim 50,000$  cells at the  
564 blastula ( $\sim 900$  embryos), gastrula ( $\sim 500$ ), elongation ( $\sim 300$ ), mitraria larva ( $\sim 150$ ) and  
565 competent larva ( $\sim 40$ ) stages following the omniATAC protocol<sup>118</sup>, but gently homogenising  
566 the samples with a pestle in lysis buffer and incubating them on ice for 3 min. Tagmentation  
567 was performed for 30 min at  $37^{\circ}\text{C}$  with an in-house purified Tn5 enzyme<sup>119</sup>. After DNA  
568 clean-up, ATAC-seq libraries were amplified as previously described. Primers used for both  
569 PCR and qPCR are listed in Supplementary Table 21. Amplified libraries were purified using  
570 ClentMag PCR Clean Up Beads as indicated by the supplier and quantified and quality  
571 checked on a Qubit 4 Fluorometer (Thermo-Fisher) and an Agilent 2200 TapeStation system  
572 before pooling at equal molecular weight. Sequencing was performed on an Illumina  
573 HiSeq4000 platform in  $2 \times 75$  bases mode at the Oxford Genomics Centre (University of  
574 Oxford, United Kingdom) (blastula, elongation and mitraria larva stages, and one replicate of  
575 gastrula) and on an Illumina NovoSeq6000 in  $2 \times 150$  bases mode at Novogene (Cambridge,  
576 United Kingdom) (one replicate of gastrula and two replicates of competent larva stages).

577

#### 578 *Chromatin accessibility profiling and motif identification and enrichment analyses*

579 We used cutadapt v.2.5<sup>120</sup> to remove sequencing adaptors and trim reads from libraries  
580 sequenced in  $2 \times 150$  bases mode to 75 bases reads. Quality filtered reads were mapped using  
581 NextGenMap v.0.5.5<sup>121</sup> in paired-end mode, duplicates were removed using samtools v.1.9<sup>122</sup>  
582 and mapped reads were shifted using deepTools v.3.4.3<sup>123</sup>. Fragment size distribution was  
583 estimated from resulting BAM files and transcription start site (TSS) enrichment analysis was  
584 computed using computeMatrix and plotHeatmap commands in deepTools v.3.4.3. Peak  
585 calling was done with MACS2 v.2.2.7.1<sup>124,125</sup> (-f BAMPE --min-length 100 --max-gap 75 and  
586 -q 0.01). Peaks from repetitive regions were filtered with BEDtools v.2.28.0<sup>126</sup> and  
587 irreproducible discovery rates (IDR) v.2.0.4.2 was used to identify reproducible peaks  
588 (IDR < 0.05) at each developmental stage. Next, we used DiffBind v.3.0.14<sup>127</sup> to generate a  
589 final consensus peak set of 47,406 peaks, which were normalised using DESeq2 analysis.  
590 Peak clustering according to accessibility dynamics was performed as described above for  
591 RNA-seq, using the same number of 12 clusters to make both profiling techniques  
592 comparable. Principal component analysis and differential accessibility analyses between  
593 consecutive developmental stages were also performed as described above. An LFC > 0 and a  
594 LFC < 0 indicates whether a peak opens or closes, respectively, given that the adjusted *p*-  
595 value < 0.05. Stage-specific and constitutive peaks were determined using UpSetR v.1.4.0<sup>128</sup>  
596 and both the consensus peak set and the stage-specific peak sets were classified by genomic  
597 feature/region using HOMER v.4.11<sup>129</sup> and further manually curated. Visualisation of peak  
598 tracks and gene structures was conducted with pyGenomeTracks v.2.1<sup>130</sup> and deepTools  
599 v.3.4.3<sup>123</sup>. To correlate chromatin accessibility and gene expression, this genomic region  
600 annotation was used to assign peaks to their closest gene and the Pearson correlation  
601 coefficient between chromatin accessibility and gene expression was computed. Promoter  
602 and intergenic peaks were subset, for which we then used GimmeMotifs v.0.16.1<sup>131</sup> to  
603 perform *de novo* motif search and differential motif enrichment in our peak sets. Data

604 clustering was performed with mfuzz v.2.52<sup>102</sup> and visualized with ComplexHeatmap package  
605 v.2.6.2<sup>132</sup>.

606

### 607 *Phylostratigraphy*

608 To evaluate gene expression dynamics by phylostratum and developmental stage, we used the  
609 OrthoFinder gene families and their inferred origins. We deemed all genes originating before  
610 and with the Cnidarian-Bilaterian ancestor of metazoan origin (Supplementary Table 27). We  
611 then applied a quantile normalisation onto the DESeq2 normalised matrix of gene expression  
612 values spanning blastula to juvenile stages. The 75 % percentile of the quantile-normalised  
613 gene expression levels was used as the summarising measure of the gene expression  
614 distribution by developmental stage. Furthermore, we tested the over- or underrepresentation  
615 of the different phylostrata in the gene expression clusters through pair-wise Fisher's exact  
616 tests, for which we then adjusted the  $p$ -values using the Bonferroni correction for multiple  
617 testing.

618

### 619 *Comparative transcriptomics*

620 Publicly available RNA-seq developmental time courses for the development of *Nematostella*  
621 *vectensis*, *Strongylocentrotus purpuratus*, *Branchiostoma lanceolatum*, *Danio rerio*,  
622 *Drosophila melanogaster*, *Caenorhabditis elegans*, and *Crassostrea gigas*, and two stages of  
623 *Capitella teleta* were downloaded from the SRA (Supplementary Table 29), cleaned for  
624 adaptors and low-quality reads with trimmomatic v.0.39<sup>74</sup> and pseudo-aligned to their  
625 respective non-redundant genome-based gene repertoires using kallisto v.0.46.2<sup>99</sup>. We then  
626 performed a quantile transformation of TPM values using scikit-learn v.1.0.2<sup>133</sup> and

627 calculated the Jensen-Shannon divergence (JSD) from single copy orthologs between all  
628 possible 1-to-1 species comparisons using the philentropy v.0.5.0 package<sup>134</sup>:

$$629 \quad JSD_{\text{raw}}(P \parallel Q) = \frac{1}{2} \sum_{i=0}^n p_i \times \log_2 \left( \frac{p_i}{\frac{1}{2}(p_i + q_i)} \right) + \frac{1}{2} \sum_{i=0}^n q_i \times \log_2 \left( \frac{q_i}{\frac{1}{2}(p_i + q_i)} \right)$$

630 Transcriptomic divergences were calculated based on 250 bootstrap replicates, from which  
631 statistically robust mean values and standard deviations were obtained. Raw mean JSD values  
632 ( $JSD_{\text{raw}}$ ) were adjusted ( $JSD_{\text{adj}}$ ) by dividing by the number of single copy orthologs of each  
633 comparison (Supplementary Table 30), and normalised using the minimum and maximum  
634 adjusted JSD values from all 1-to-1 species comparisons as follows:

$$635 \quad JSD_{\text{norm}}(P \parallel Q) = \frac{JSD_{\text{adj}}(P \parallel Q) - \min JSD_{\text{adj}}}{\max JSD_{\text{adj}} - \min JSD_{\text{adj}}}; JSD_{\text{norm}} \in (0, 1)$$

636 Relative JSD values were obtained equally, using minimum and maximum adjusted JSD  
637 values from each 1-to-1 species comparison instead. For a further analysis with a subset of  
638 common orthologues, raw mean JSD values needed no adjustment for comparison purposes.

639

## 640 **References**

- 641 1 Hall, B. K. & Wake, M. H. in *The Origin and Evolution of Larval Forms* (eds Brian  
642 K. Hall & Marvalee H. Wake) Ch. 1, 1-19 (Academic Press, 1999).
- 643 2 Nielsen, C. Origin and evolution of animal life cycles. *Biol Rev* **73**, 125-155 (1998).
- 644 3 Nielsen, C. Animal phylogeny in the light of the trochaea theory. *Biological Journal*  
645 *of the Linnean Society* **25**, 243-299 (2008).
- 646 4 Garstang, W. The origin and evolution of larval forms. 77-98 (British Association for  
647 the Advancement of Science, London, 1928).

648 5 Jägersten, G. *Evolution of the Metazoan Life Cycle*. (Academic Press, 1972).

649 6 Marlow, H. *et al.* Larval body patterning and apical organs are conserved in animal  
650 evolution. *BMC Biol* **12**, 7 (2014).

651 7 Wang, J. *et al.* Evolutionary transcriptomics of metazoan biphasic life cycle supports  
652 a single intercalation origin of metazoan larvae. *Nat Ecol Evol* **4**, 725-736 (2020).

653 8 Salvini-Plawen, L. v. On the origin and evolution of the lower Metazoa. *Z Zool Syst*  
654 *Evol Forsch* **16**, 40-87 (1978).

655 9 Hazsprunar, G., Salvini-Plawen, L. v. & Rieger, R. M. Larval Planktotrophy — A  
656 Primitive Trait in the Bilateria? *Acta Zoologica* **76**, 141-154 (1995).

657 10 Raff, R. A. Origins of the other metazoan body plans: the evolution of larval forms.  
658 *Philos Trans R Soc Lond B Biol Sci* **363**, 1473-1479 (2008).

659 11 Sly, B. J., Snoke, M. S. & Raff, R. A. Who came first - larvae or adults? Origins of  
660 bilaterian metazoan larvae. *Int J Dev Biol* **47**, 623-632 (2003).

661 12 Davidson, E. H., Peterson, K. J. & Cameron, R. A. Origin of bilaterian body plans:  
662 evolution of developmental regulatory mechanisms. *Science* **270**, 1319-1325 (1995).

663 13 Rouse, G. W., Pleijel, F. & Tilic, E. *Annelida*. (Oxford University Press, 2022).

664 14 Lacalli, T. C. Protochordate body plan and the evolutionary role of larvae: old  
665 controversies resolved? *Can. J. Zool.* **83**, 216-224 (2005).

666 15 Strathman, R. Multiple origins of feeding head larvae by the Early Cambrian. *Can. J.*  
667 *Zool.* **98**, 761-776 (2020).

668 16 Hatschek, B. Studien über Entwicklungsgeschichte der Anneliden. Ein Beitrag zur  
669 Morphologie der Bilaterien. *Arbeiten aus dem Zoologischen Institute der Universität*  
670 *Wien und der Zoologischen Station in Triest* **1**, 277-404 (1878).

671 17 Rouse, G. W. Trochophore concepts: ciliary bands and the evolution of larvae in  
672 spiralian Metazoa. *Biological Journal of the Linnean Society* **66**, 411-464 (2008).

- 673 18 Marlétaz, F., Peijnenburg, K., Goto, T., Satoh, N. & Rokhsar, D. S. A New Spiralian  
674 Phylogeny Places the Enigmatic Arrow Worms among Gnathiferans. *Curr Biol* **29**,  
675 312-318 e313 (2019).
- 676 19 Nielsen, C. *Animal Evolution. Interrelationships of the Living Phyla*. 3rd edn,  
677 (Oxford University Press, 2012).
- 678 20 Nielsen, C. Evolution of deuterostomy - and origin of the chordates. *Biol Rev Camb*  
679 *Philos Soc* **92**, 316-325 (2017).
- 680 21 Wilson, D. P. IV. On the Mitraria Larva of *Owenia fusiformis* Delle Chiaje.  
681 *Philosophical Transactions of the Royal Society of London. Series B, Containing*  
682 *Papers of a Biological Character* **221**, 231-334 (1932).
- 683 22 Nielsen, C. Trochophora larvae: cell-lineages, ciliary bands and body regions. 2.  
684 Other groups and general discussion. *J Exp Zool B Mol Dev Evol* **304**, 401-447  
685 (2005).
- 686 23 Smart, T. I. & Von Dassow, G. Unusual development of the mitraria larva in the  
687 polychaete *Owenia collaris*. *Biol Bull* **217**, 253-268 (2009).
- 688 24 Gasiorowski, L. *et al.* Molecular evidence for a single origin of ultrafiltration-based  
689 excretory organs. *Curr Biol* **31**, 3629-3638 e3622 (2021).
- 690 25 Carrillo-Baltodano, A. M., Seudre, O., Guynes, K. & Martin-Duran, J. M. Early  
691 embryogenesis and organogenesis in the annelid *Owenia fusiformis*. *Evodevo* **12**, 5  
692 (2021).
- 693 26 Seudre, O., Carrillo-Baltodano, A. M., Liang, Y. & Martín-Durán, J. M. ERK1/2 is an  
694 ancestral organising signal in spiral cleavage. *bioRxiv*, 2021.2005.2026.445819  
695 (2021).
- 696 27 Martin-Duran, J. M. *et al.* Convergent evolution of bilaterian nerve cords. *Nature* **553**,  
697 45-50 (2018).

- 698 28 Martin-Duran, J. M., Passamanek, Y. J., Martindale, M. Q. & Hejnol, A. The  
699 developmental basis for the recurrent evolution of deuterostomy and protostomy. *Nat*  
700 *Ecol Evol* **1**, 5 (2016).
- 701 29 Simakov, O. *et al.* Insights into bilaterian evolution from three spiralian genomes.  
702 *Nature* **493**, 526-531 (2013).
- 703 30 Wang, S. *et al.* Scallop genome provides insights into evolution of bilaterian  
704 karyotype and development. *Nat Ecol Evol* **1**, 120 (2017).
- 705 31 Martin-Duran, J. M. *et al.* Conservative route to genome compaction in a miniature  
706 annelid. *Nat Ecol Evol* **5**, 231-242 (2021).
- 707 32 Shao, Y. *et al.* Genome and single-cell RNA-sequencing of the earthworm *Eisenia*  
708 *andrei* identifies cellular mechanisms underlying regeneration. *Nat Commun* **11**, 2656  
709 (2020).
- 710 33 Niehrs, C. On growth and form: a Cartesian coordinate system of Wnt and BMP  
711 signaling specifies bilaterian body axes. *Development* **137**, 845-857 (2010).
- 712 34 Tan, S., Huan, P. & Liu, B. Molluscan dorsal-ventral patterning relying on BMP2/4  
713 and Chordin provides insights into spiralian development and evolution. *Mol Biol*  
714 *Evol* (2021).
- 715 35 Lyons, D. C., Perry, K. J., Batzel, G. & Henry, J. Q. BMP signaling plays a role in  
716 anterior-neural/head development, but not organizer activity, in the gastropod  
717 *Crepidula fornicata*. *Dev Biol* **463**, 135-157 (2020).
- 718 36 Pearson, J. C., Lemons, D. & McGinnis, W. Modulating Hox gene functions during  
719 animal body patterning. *Nat Rev Genet* **6**, 893-904, doi:10.1038/nrg1726 (2005).
- 720 37 Fröblius, A. C., Matus, D. Q. & Seaver, E. C. Genomic organization and expression  
721 demonstrate spatial and temporal Hox gene colinearity in the lophotrochozoan  
722 *Capitella* sp. I. *PLoS One* **3**, e4004 (2008).



723 38 Hui, J. H. *et al.* Extensive chordate and annelid macrosynteny reveals ancestral  
724 homeobox gene organization. *Mol Biol Evol* **29**, 157-165 (2012).

725 39 Kulakova, M. *et al.* Hox gene expression in larval development of the polychaetes  
726 *Nereis virens* and *Platynereis dumerilii* (Annelida, Lophotrochozoa). *Dev Genes Evol*  
727 **217**, 39-54 (2007).

728 40 Woltereck, R. Trochophora-Studien I. Histologie der larve und die Entstehung des  
729 Annelids bei den *Polygordius*-Arten der Nordsee. *Zoologica* **13** (1902).

730 41 Simionato, E. *et al.* *atonal*- and *achaete-scute*-related genes in the annelid *Platynereis*  
731 *dumerilii*: insights into the evolution of neural basic-Helix-Loop-Helix genes. *BMC*  
732 *Evol Biol* **8**, 170 (2008).

733 42 Wu, L., Ferger, K. E. & Lambert, J. D. Gene Expression Does Not Support the  
734 Developmental Hourglass Model in Three Animals with Spiralian Development. *Mol*  
735 *Biol Evol* **36**, 1373-1383 (2019).

736 43 Wu, L. *et al.* Genes with spiralian-specific protein motifs are expressed in spiralian  
737 ciliary bands. *Nat Commun* **11**, 4171 (2020).

738 44 Marinković, M., Berger, J. & Jékely, G. Neuronal coordination of motile cilia in  
739 locomotion and feeding. *Philos Trans R Soc Lond B Biol Sci* **375**, 20190165 (2020).

740 45 Irvine, S. Q. & Martindale, M. Q. Expression patterns of anterior Hox genes in the  
741 polychaete *Chaetopterus*: correlation with morphological boundaries. *Dev Biol* **217**,  
742 333-351 (2000).

743 46 Peterson, K. J., Irvine, S. Q., Cameron, R. A. & Davidson, E. H. Quantitative  
744 assessment of *Hox* complex expression in the indirect development of the polychaete  
745 annelid *Chaetopterus* sp. *Proc Natl Acad Sci U S A* **97**, 4487-4492 (2000).

746 47 Weigert, A. *et al.* Illuminating the base of the annelid tree using transcriptomics. *Mol*  
747 *Biol Evol* **31**, 1391-1401 (2014).

748 48 Hiebert, L. S. & Maslakova, S. A. *Hox* genes pattern the anterior-posterior axis of the  
749 juvenile but not the larva in a maximally indirect developing invertebrate, *Micrura*  
750 *alaskensis* (Nemertea). *BMC Biol* **13**, 23 (2015).

751 49 Gasiorowski, L. & Hejnal, A. *Hox* gene expression during development of the  
752 phoronid *Phoronopsis harmeri*. *Evodevo* **11**, 2 (2020).

753 50 Brenneis, G., Bogomolova, E. V., Arango, C. P. & Krapp, F. From egg to "no-body":  
754 an overview and revision of developmental pathways in the ancient arthropod lineage  
755 Pycnogonida. *Front Zool* **14**, 6 (2017).

756 51 Arenas-Mena, C., Cameron, A. R. & Davidson, E. H. Spatial expression of *Hox*  
757 cluster genes in the ontogeny of a sea urchin. *Development* **127**, 4631-4643 (2000).

758 52 Arenas-Mena, C., Martinez, P., Cameron, R. A. & Davidson, E. H. Expression of the  
759 *Hox* gene complex in the indirect development of a sea urchin. *Proc Natl Acad Sci U*  
760 *S A* **95**, 13062-13067 (1998).

761 53 Gonzalez, P., Uhlinger, K. R. & Lowe, C. J. The Adult Body Plan of Indirect  
762 Developing Hemichordates Develops by Adding a *Hox*-Patterned Trunk to an  
763 Anterior Larval Territory. *Curr Biol* **27**, 87-95 (2017).

764 54 Aronowicz, J. & Lowe, C. J. *Hox* gene expression in the hemichordate *Saccoglossus*  
765 *kowalevskii* and the evolution of deuterostome nervous systems. *Integr Comp Biol* **46**,  
766 890-901 (2006).

767 55 Pascual-Anaya, J. *et al.* Broken colinearity of the amphioxus *Hox* cluster. *Evodevo* **3**,  
768 28 (2012).

769 56 Carrillo-Baltodano, A. M. & Meyer, N. P. Decoupling brain from nerve cord  
770 development in the annelid *Capitella teleta*: Insights into the evolution of nervous  
771 systems. *Dev Biol* **431**, 134-144 (2017).

772 57 Luo, Y. J. *et al.* Nemertean and phoronid genomes reveal lophotrochozoan evolution  
773 and the origin of bilaterian heads. *Nat Ecol Evol* **2**, 141-151 (2018).

774 58 Steinmetz, P. R. *et al.* *Six3* demarcates the anterior-most developing brain region in  
775 bilaterian animals. *Evodevo* **1**, 14 (2010).

776 59 Hiebert, L. S. & Maslakova, S. A. Expression of *Hox*, *Cdx*, and *Six3/6* genes in the  
777 hoplonemertean *Pantionemertes californiensis* offers insight into the evolution of  
778 maximally indirect development in the phylum Nemertea. *Evodevo* **6**, 26 (2015).

779 60 Seaver, E. C., Thamm, K. & Hill, S. D. Growth patterns during segmentation in the  
780 two polychaete annelids, *Capitella* sp. I and *Hydroides elegans*: comparisons at  
781 distinct life history stages. *Evol Dev* **7**, 312-326 (2005).

782 61 Marçais, G. & Kingsford, C. A fast, lock-free approach for efficient parallel counting  
783 of occurrences of *k*-mers. *Bioinformatics* **27**, 764-770 (2011).

784 62 Ranallo-Benavidez, T. R., Jaron, K. S. & Schatz, M. C. GenomeScope 2.0 and  
785 Smudgeplot for reference-free profiling of polyploid genomes. *Nat Commun* **11**, 1432  
786 (2020).

787 63 Koren, S. *et al.* Canu: scalable and accurate long-read assembly via adaptive k-mer  
788 weighting and repeat separation. *Genome Res* **27**, 722-736,  
789 doi:10.1101/gr.215087.116 (2017).

790 64 Li, H. Aligning sequence reads, clone sequences and assembly contigs with BWA-  
791 MEM. *arXiv* **1303.3997** (2013).

792 65 Vaser, R., Sovic, I., Nagarajan, N. & Sikic, M. Fast and accurate de novo genome  
793 assembly from long uncorrected reads. *Genome Res* **27**, 737-746 (2017).

794 66 Roach, M. J., Schmidt, S. A. & Borneman, A. R. Purge Haplotigs: allelic contig  
795 reassignment for third-gen diploid genome assemblies. *BMC Bioinformatics* **19**, 460  
796 (2018).

797 67 Rhie, A., Walenz, B. P., Koren, S. & Phillippy, A. M. Merqury: reference-free  
798 quality, completeness, and phasing assessment for genome assemblies. *Genome Biol*  
799 **21**, 245 (2020).

800 68 Manni, M., Berkeley, M. R., Seppey, M., Simao, F. A. & Zdobnov, E. M. BUSCO  
801 Update: Novel and Streamlined Workflows along with Broader and Deeper  
802 Phylogenetic Coverage for Scoring of Eukaryotic, Prokaryotic, and Viral Genomes.  
803 *Mol Biol Evol* **38**, 4647-4654 (2021).

804 69 Flynn, J. M. *et al.* RepeatModeler2 for automated genomic discovery of transposable  
805 element families. *Proc Natl Acad Sci U S A* **117**, 9451-9457 (2020).

806 70 Xu, Z. & Wang, H. LTR\_FINDER: an efficient tool for the prediction of full-length  
807 LTR retrotransposons. *Nucleic Acids Res* **35**, W265-268 (2007).

808 71 Wong, W. Y. & Simakov, O. RepeatCraft: a meta-pipeline for repetitive element de-  
809 fragmentation and annotation. *Bioinformatics* **35**, 1051-1052 (2019).

810 72 Danecek, P. *et al.* Twelve years of SAMtools and BCFtools. *Gigascience* **10** (2021).

811 73 Dobin, A. *et al.* STAR: ultrafast universal RNA-seq aligner. *Bioinformatics* **29**, 15-21  
812 (2013).

813 74 Bolger, A. M., Lohse, M. & Usadel, B. Trimmomatic: a flexible trimmer for Illumina  
814 sequence data. *Bioinformatics* **30**, 2114-2120 (2014).

815 75 Pertea, M. *et al.* StringTie enables improved reconstruction of a transcriptome from  
816 RNA-seq reads. *Nat Biotechnol* **33**, 290-295 (2015).

817 76 Mapleson, D., Venturini, L., Kaithakottil, G. & Swarbreck, D. Efficient and accurate  
818 detection of splice junctions from RNA-seq with Portcullis. *Gigascience* **7** (2018).

819 77 Grabherr, M. G. *et al.* Full-length transcriptome assembly from RNA-Seq data  
820 without a reference genome. *Nat Biotechnol* **29**, 644-652 (2011).

821 78 Wu, T. D. & Watanabe, C. K. GMAP: a genomic mapping and alignment program for  
822 mRNA and EST sequences. *Bioinformatics* **21**, 1859-1875 (2005).

823 79 Venturini, L., Caim, S., Kaithakottil, G. G., Mapleson, D. L. & Swarbreck, D.  
824 Leveraging multiple transcriptome assembly methods for improved gene structure  
825 annotation. *Gigascience* **7** (2018).

826 80 Stanke, M., Schoffmann, O., Morgenstern, B. & Waack, S. Gene prediction in  
827 eukaryotes with a generalized hidden Markov model that uses hints from external  
828 sources. *BMC Bioinformatics* **7**, 62 (2006).

829 81 Slater, G. S. & Birney, E. Automated generation of heuristics for biological sequence  
830 comparison. *BMC Bioinformatics* **6**, 31 (2005).

831 82 Haas, B. J. *et al.* Improving the *Arabidopsis* genome annotation using maximal  
832 transcript alignment assemblies. *Nucleic Acids Res* **31**, 5654-5666 (2003).

833 83 Camacho, C. *et al.* BLAST+: architecture and applications. *BMC Bioinformatics* **10**,  
834 421 (2009).

835 84 Bryant, D. M. *et al.* A Tissue-Mapped Axolotl De Novo Transcriptome Enables  
836 Identification of Limb Regeneration Factors. *Cell Rep* **18**, 762-776 (2017).

837 85 Eddy, S. R. Accelerated Profile HMM Searches. *PLoS Comput Biol* **7**, e1002195  
838 (2011).

839 86 Petersen, T. N., Brunak, S., von Heijne, G. & Nielsen, H. SignalP 4.0: discriminating  
840 signal peptides from transmembrane regions. *Nat Methods* **8**, 785-786 (2011).

841 87 Mi, H. *et al.* PANTHER version 16: a revised family classification, tree-based  
842 classification tool, enhancer regions and extensive API. *Nucleic Acids Res* **49**, D394-  
843 D403 (2021).

844 88 Durand, N. C. *et al.* Juicer Provides a One-Click System for Analyzing Loop-  
845 Resolution Hi-C Experiments. *Cell Syst* **3**, 95-98 (2016).

846 89 Dudchenko, O. *et al.* De novo assembly of the *Aedes aegypti* genome using Hi-C  
847 yields chromosome-length scaffolds. *Science* **356**, 92-95 (2017).

848 90 Shumate, A. & Salzberg, S. L. Liftoff: accurate mapping of gene annotations.  
849 *Bioinformatics* **37**, 1639-1643 (2021).

850 91 Emms, D. M. & Kelly, S. OrthoFinder: phylogenetic orthology inference for  
851 comparative genomics. *Genome Biol* **20**, 238 (2019).

852 92 Steinegger, M. & Soding, J. MMseqs2 enables sensitive protein sequence searching  
853 for the analysis of massive data sets. *Nat Biotechnol* **35**, 1026-1028 (2017).

854 93 Huerta-Cepas, J., Serra, F. & Bork, P. ETE 3: Reconstruction, Analysis, and  
855 Visualization of Phylogenomic Data. *Mol Biol Evol* **33**, 1635-1638 (2016).

856 94 Marletaz, F. *et al.* Amphioxus functional genomics and the origins of vertebrate gene  
857 regulation. *Nature* **564**, 64-70 (2018).

858 95 Zeng, Q. *et al.* High-quality reannotation of the king scallop genome reveals no 'gene-  
859 rich' feature and evolution of toxin resistance. *Comput Struct Biotechnol J* **19**, 4954-  
860 4960 (2021).

861 96 Zakas, C., Harry, N. D., Scholl, E. H. & Rockman, M. V. The genome of the  
862 poecilogonous annelid *Streblospio benedicti*. *Genome Biology and Evolution* (2022).

863 97 Kwiatkowski, D. *et al.* The genome sequence of the bootlace worm, *Lineus*  
864 *longissimus* (Gunnerus, 1770). *Wellcome Open Res* **6**, 272 (2021).

865 98 Cannon, J. T. *et al.* Xenacoelomorpha is the sister group to Nephrozoa. *Nature* **530**,  
866 89-93 (2016).

867 99 Bray, N. L., Pimentel, H., Melsted, P. & Pachter, L. Near-optimal probabilistic RNA-  
868 seq quantification. *Nat Biotechnol* **34**, 525-527 (2016).

869 100 Love, M. I., Huber, W. & Anders, S. Moderated estimation of fold change and  
870 dispersion for RNA-seq data with DESeq2. *Genome Biol* **15**, 550 (2014).

871 101 Park, C. *et al.* The developmental transcriptome atlas of the spoon worm *Urechis*  
872 *unicinctus* (Echiurida: Annelida). *Gigascience* **7**, 1-7 (2018).

873 102 Futschik, M. E. & Carlisle, B. Noise-robust soft clustering of gene expression time-  
874 course data. *J Bioinform Comput Biol* **3**, 965-988 (2005).

875 103 Langfelder, P. & Horvath, S. WGCNA: an R package for weighted correlation  
876 network analysis. *BMC Bioinformatics* **9**, 559 (2008).

877 104 Shannon, P. *et al.* Cytoscape: a software environment for integrated models of  
878 biomolecular interaction networks. *Genome Res* **13**, 2498-2504 (2003).

879 105 Gu, Z. & Hübschmann, D. simplifyEnrichment: an R/Bioconductor package for  
880 Clustering and Visualizing Functional Enrichment Results. *bioRxiv*,  
881 2020.2010.2027.312116 (2021).

882 106 Katoh, K. & Standley, D. M. MAFFT multiple sequence alignment software version  
883 7: improvements in performance and usability. *Mol Biol Evol* **30**, 772-780,  
884 doi:10.1093/molbev/mst010 (2013).

885 107 Katoh, K. & Frith, M. C. Adding unaligned sequences into an existing alignment  
886 using MAFFT and LAST. *Bioinformatics* **28**, 3144-3146 (2012).

887 108 Whelan, S. & Goldman, N. A general empirical model of protein evolution derived  
888 from multiple protein families using a maximum-likelihood approach. *Mol Biol Evol*  
889 **18**, 691-699 (2001).

890 109 Soubrier, J. *et al.* The influence of rate heterogeneity among sites on the time  
891 dependence of molecular rates. *Mol Biol Evol* **29**, 3345-3358 (2012).

892 110 Nguyen, L. T., Schmidt, H. A., von Haeseler, A. & Minh, B. Q. IQ-TREE: a fast and  
893 effective stochastic algorithm for estimating maximum-likelihood phylogenies. *Mol*  
894 *Biol Evol* **32**, 268-274 (2015).

895 111 Hoang, D. T., Chernomor, O., von Haeseler, A., Minh, B. Q. & Vinh, L. S. UFBoot2:  
896 Improving the Ultrafast Bootstrap Approximation. *Mol Biol Evol* **35**, 518-522 (2018).

897 112 Ronquist, F. & Huelsenbeck, J. P. MrBayes 3: Bayesian phylogenetic inference under  
898 mixed models. *Bioinformatics* **19**, 1572-1574 (2003).

899 113 Yang, Z. Maximum likelihood phylogenetic estimation from DNA sequences with  
900 variable rates over sites: approximate methods. *J Mol Evol* **39**, 306-314 (1994).

901 114 Talavera, G. & Castresana, J. Improvement of phylogenies after removing divergent  
902 and ambiguously aligned blocks from protein sequence alignments. *Syst Biol* **56**, 564-  
903 577 (2007).

904 115 Stamatakis, A. RAxML version 8: a tool for phylogenetic analysis and post-analysis  
905 of large phylogenies. *Bioinformatics* **30**, 1312-1313 (2014).

906 116 Le, S. Q. & Gascuel, O. An improved general amino acid replacement matrix. *Mol*  
907 *Biol Evol* **25**, 1307-1320 (2008).

908 117 Meyer, N. P., Carrillo-Baltodano, A., Moore, R. E. & Seaver, E. C. Nervous system  
909 development in lecithotrophic larval and juvenile stages of the annelid *Capitella*  
910 *teleta*. *Front Zool* **12**, 15 (2015).

911 118 Corces, M. R. *et al.* An improved ATAC-seq protocol reduces background and  
912 enables interrogation of frozen tissues. *Nat Methods* **14**, 959-962 (2017).

913 119 Picelli, S. *et al.* Tn5 transposase and tagmentation procedures for massively scaled  
914 sequencing projects. *Genome Res* **24**, 2033-2040 (2014).

915 120 Martin, M. Cutadapt removes adapter sequences from high-throughput sequencing  
916 reads. *2011* **17**, 3 (2011).

917 121 Sedlazeck, F. J., Rescheneder, P. & von Haeseler, A. NextGenMap: fast and accurate  
918 read mapping in highly polymorphic genomes. *Bioinformatics* **29**, 2790-2791 (2013).



919 122 Li, H. *et al.* The Sequence Alignment/Map format and SAMtools. *Bioinformatics* **25**,  
920 2078-2079 (2009).

921 123 Ramirez, F. *et al.* deepTools2: a next generation web server for deep-sequencing data  
922 analysis. *Nucleic Acids Res* **44**, W160-165 (2016).

923 124 Gaspar, J. M. Improved peak-calling with MACS2. *bioRxiv*, 496521 (2018).

924 125 Zhang, Y. *et al.* Model-based analysis of ChIP-Seq (MACS). *Genome Biol* **9**, R137  
925 (2008).

926 126 Quinlan, A. R. & Hall, I. M. BEDTools: a flexible suite of utilities for comparing  
927 genomic features. *Bioinformatics* **26**, 841-842 (2010).

928 127 Ross-Innes, C. S. *et al.* Differential oestrogen receptor binding is associated with  
929 clinical outcome in breast cancer. *Nature* **481**, 389-393 (2012).

930 128 Conway, J. R., Lex, A. & Gehlenborg, N. UpSetR: an R package for the visualization  
931 of intersecting sets and their properties. *Bioinformatics* **33**, 2938-2940 (2017).

932 129 Heinz, S. *et al.* Simple combinations of lineage-determining transcription factors  
933 prime *cis*-regulatory elements required for macrophage and B cell identities. *Mol Cell*  
934 **38**, 576-589 (2010).

935 130 Lopez-Delisle, L. *et al.* pyGenomeTracks: reproducible plots for multivariate genomic  
936 datasets *Bioinformatics* **37**, 422-423 (2020).

937 131 van Heeringen, S. J. & Veenstra, G. J. GimmeMotifs: a *de novo* motif prediction  
938 pipeline for ChIP-sequencing experiments. *Bioinformatics* **27**, 270-271 (2011).

939 132 Gu, Z., Eils, R. & Schlesner, M. Complex heatmaps reveal patterns and correlations in  
940 multidimensional genomic data. *Bioinformatics* **32**, 2847-2849 (2016).

941 133 Pedregosa, F. *et al.* Scikit-learn: Machine Learning in Python. *Journal of Machine*  
942 *Learning Research* **12**, 2825–2830 (2011).

943 134 Drost, H. G. Philentropy: Information Theory and Distance Quantification with R.  
944 *Journal of Open Source Software* **3**, 765 (2018).

945

## 946 **Acknowledgments**

947 We thank Alex de Mendoza and Daria Gavriouchkina for their support and valuable  
948 comments on the manuscript, as well as the staff at Station Biologique de Roscoff for their  
949 help with collections and animal supplies and the Oxford Genomics Centre at the Wellcome  
950 Centre for Human Genetics (funded by Wellcome Trust grant reference 203141/Z/16/Z) for  
951 the generation and initial processing of RNA-seq and ATAC-seq sequencing data. We also  
952 thank Michael J Boyle for providing the *chordin* sequence for *Themiste lageniformis*, Joseph  
953 Deane for initial help with *Hox* gene characterisation in *O. fusiformis*, and the core technical  
954 staff at the Department of Biology at Queen Mary University of London for their constant  
955 support. This work used computing resources from Queen Mary University of London's  
956 Apocrita HPC facilities. This work was funded by the Horizon 2020 Framework Programme  
957 to JMM-D (European Research Council Starting Grant action number 801669) and AH  
958 (European Research Council Consolidator Grant action number 648861) and a Royal Society  
959 University Research Fellowship (URF\R1\191161) and a Japan Society for the Promotion of  
960 Science Kakenhi grant (JP 19K06620) to FM.

961

## 962 **Author Contributions**

963 JMM-D, FM, YL and FMM-Z conceived and designed the study; YL collected RNA-seq  
964 samples for *O. fusiformis* and *C. teleta*, performed ATAC-seq experiments and contributed to  
965 all data analyses; FMM-Z performed *chordin* orthology studies and contributed to all data  
966 analyses; KG conducted *in situ* hybridisation analyses of *Hox* genes; AC-B collected RNA-

967 seq samples for *C. teleta*, performed immunostainings on larvae and gene expression analyses  
968 of *chordin*; YT performed OMNI-C libraries; GM performed repeat annotations and  
969 analyses; OS identified and performed *in silico* analyses of *Hox* genes; MT performed  
970 genomic extractions and optical mapping; KM collected *Magelona* spp.; AH and NML  
971 contributed to sequencing efforts; FM and JMM-D assembled and annotated the genome and  
972 contributed to data analyses; YL, FMM-Z and JMM-D drafted the manuscript and all authors  
973 critically read and commented on the manuscript.

974

#### 975 **Competing Interests**

976 The authors declare no competing interests.

977

#### 978 **Data availability**

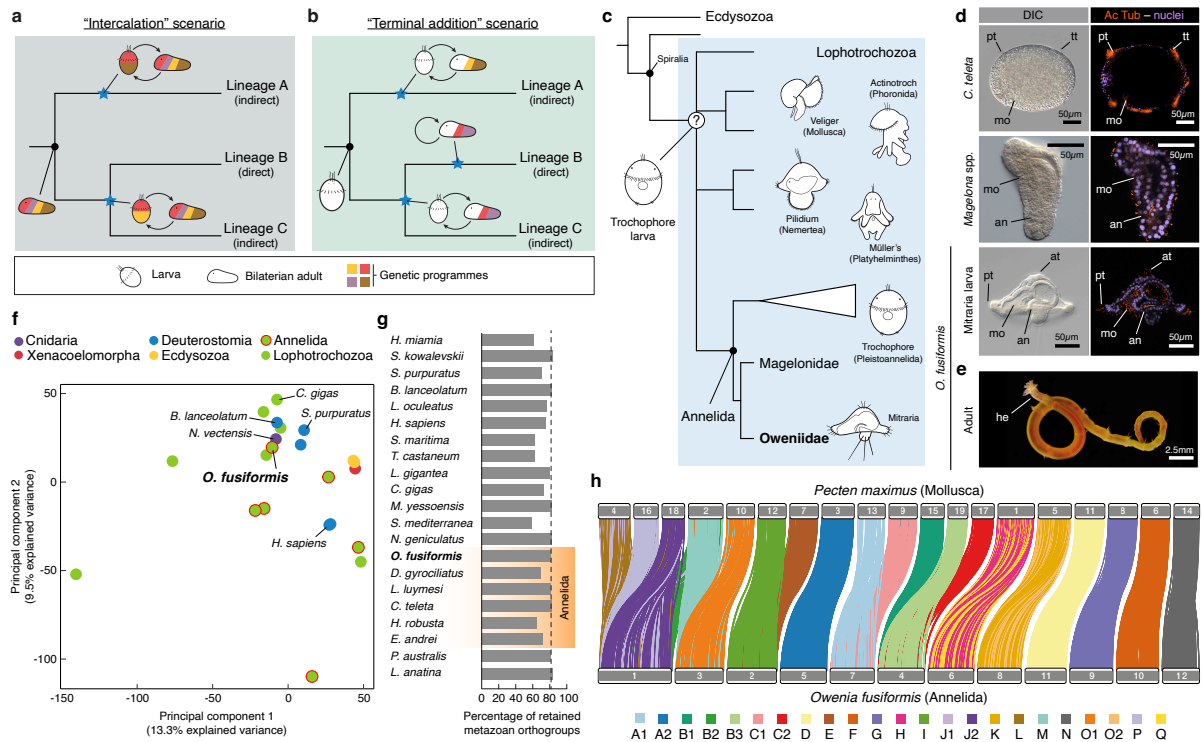
979 All sequence data associated with this project are available at the European Nucleotide  
980 Archive (project PRJEB38497) and Gene Expression Omnibus (accession numbers  
981 GSE184126 and GSE192478). Genome assemblies, transposable element annotations,  
982 genome annotation files used for RNA-seq and ATAC-seq analyses, WGCNA nodes and  
983 edges files, alignment files used in orthology assignment, and other additional files are  
984 publicly available in <https://github.com/ChemaMD/OweniaGenome>.

985

#### 986 **Code availability**

987 No custom code was used in this study.

988

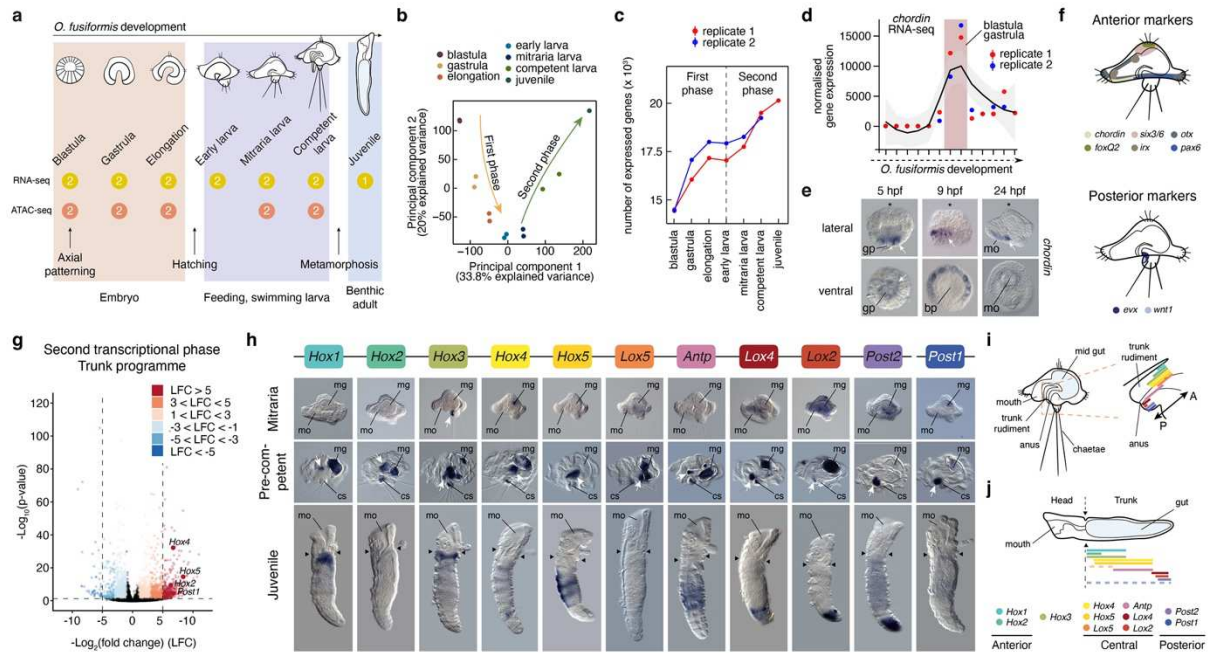


990

991 **Figure 1 | *Owenia fusiformis* has a unique larva and a conservatively evolving genome.**

992 **a, b**, Major scenarios for the evolution of bilaterian life cycles and larval forms. The  
 993 “intercalation” scenario (**a**) deems bilaterian adults ancestral and larvae secondary  
 994 specialisations that evolved independently in certain lineages by co-opting genetic  
 995 programmes (highlighted with different colours) originally expressed in the adult. The  
 996 “terminal addition” scenario (**b**) considers that bilaterian larvae are ancestral and that adult  
 997 forms evolved secondarily by incorporating new genetic programmes (indicated with  
 998 different colours) after the larval stage. Direct development (as in lineage B) would have then  
 999 evolved by losing the ancestral larval stage. **c**, A trochophore larval type has been proposed  
 1000 to be ancestral to Spiralia or even Protostomia (Ecdysozoan + Spiralia) and give rise to the  
 1001 diversity of larval forms found in lophotrochozoan taxa. **d**, The larval forms of oweniids and  
 1002 magelonids are unlike other annelid larvae. Differential interface contrast (DIC) images and  
 1003 z-stack confocal laser scanning views of a stage 5 metatrochophore of *C. teleta*, a

1004 *Magelona* spp. larva, and a *O. fusiformis* mitraria stained for DAPI and acetylated  $\alpha$ -tubulin.  
1005 **e**, Image of an adult of *O. fusiformis*. **f**, Principal component analysis of metazoan gene  
1006 complements demonstrates that *Owenia* clusters with other slow-evolving lineages. See  
1007 Extended Data Fig. 2g for a fully labelled graph. **g**, Percentage of retained pre-metazoan and  
1008 metazoan orthogroups per species. Dotted vertical line represents the value for *O. fusiformis*.  
1009 **h**, Karyotypic correspondence between *O. fusiformis* and *Pecten maximus*, which exemplifies  
1010 the ancestral spiralian chromosome complement. Each colour represents an ancestral  
1011 bilaterian linkage group. Schematic drawings are not to scale. at: apical tuft; an: anus; he:  
1012 head; mo: mouth; pt: prototroch; tt: telotroch.



1013

1014

**Figure 2 | Two transcriptional phases underpin larva embryogenesis and**

1015

**metamorphosis. a**, Schematic representation of *O. fusiformis* development from blastula to

1016

juvenile indicating major developmental events and the time points when RNA-seq and

1017

ATAC-seq samples were collected. Numbers inside the coloured circles indicate the number

1018

of biological replicates. **b**, Principal component analysis of the developmental RNA-seq time

1019

course. **c**, Number of expressed genes during *O. fusiformis* development. **d**, Expression levels

1020

of *chordin*, which peaks at the blastula and gastrula stages, after the specification and

1021

inductive activity of the embryonic organiser. **e**, Whole mount *in situ* hybridisation of

1022

*chordin* at the blastula (5 hours post fertilisation, hpf), gastrula (9 hpf), and mitraria larva

1023

(27 hpf) stages. Asterisks mark the animal/anterior pole. gp: gastral plate; bp: blastopore, mo:

1024

mouth. **f**, Schematic representation of the expression of anterior and posterior ectodermal

1025

gene markers at the mitraria stage, demonstrating how anterior territories expand throughout

1026

most of the larva. **g**, Volcano plot of the mitraria to competent larva transition, highlighting

1027

the marked upregulation of certain *Hox* genes. **h**, Whole mount *in situ* hybridisation of *Hox*

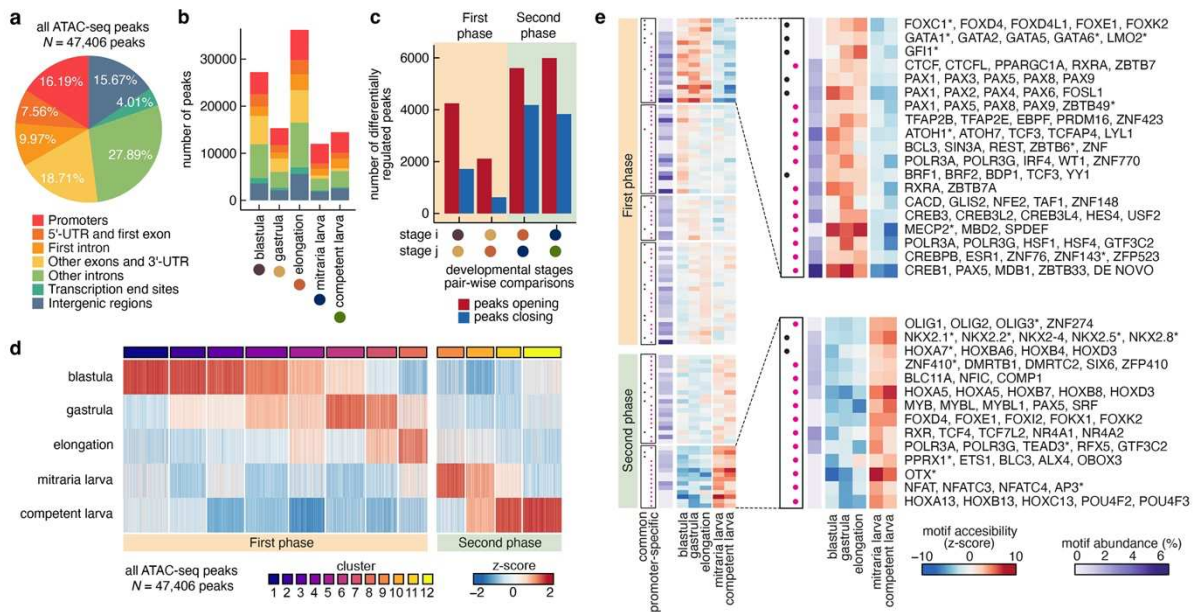
1028

genes at the mitraria, pre-competent, and juvenile stages. Only *Hox3* appears to be expressed

1029

at the mitraria stage (white arrow), while *Hox* genes show spatial collinearity along the

1030 anterior-posterior axis at the developing trunk (white arrows in the pre-competent larva) and  
1031 juvenile. Dotted lines in the competent larva panels indicate background from the gut content.  
1032 Black arrowheads in the juvenile panels indicate head to trunk boundary. cs: chaetal sack;  
1033 mg: mid gut; mo: mouth. **i, j**, Schematic representations of the expression of *Hox* genes in the  
1034 trunk rudiment of the competent larva (**i**) and juvenile trunk (**j**). A: anterior; P: posterior.  
1035 Drawings are not to scale, and schematic expression domains are approximate.



1036

1037 **Figure 3 | Chromatin dynamics support two regulatory modules during *Owenia***

1038 **development.** **a**, Genomic feature annotation of the consensus ATAC-seq peak set.

1039 **b**, Stacked bar plot showing the number of called peaks per developmental stage, classified

1040 by genomic feature. **c**, Differentially accessible peaks for all four pairwise comparisons

1041 between adjacent stages. Only significant differentially regulated peaks (adjusted  $p$ -

1042 value  $< 0.05$ ) are shown. **d**, Heatmap of normalised peak accessibility (z-score) of the soft

1043 clustered consensus ATAC-seq peaks, subdivided into clusters of open chromatin regions that

1044 peak pre- and post-larval stages. **e**, Motif enrichment analysis of promoter peaks. The

1045 clustered heatmap shows normalised motif accessibility (z-score) and the abundance of the

1046 motif in promoter peaks, subdivided in clusters of motifs mostly accessible either pre- or

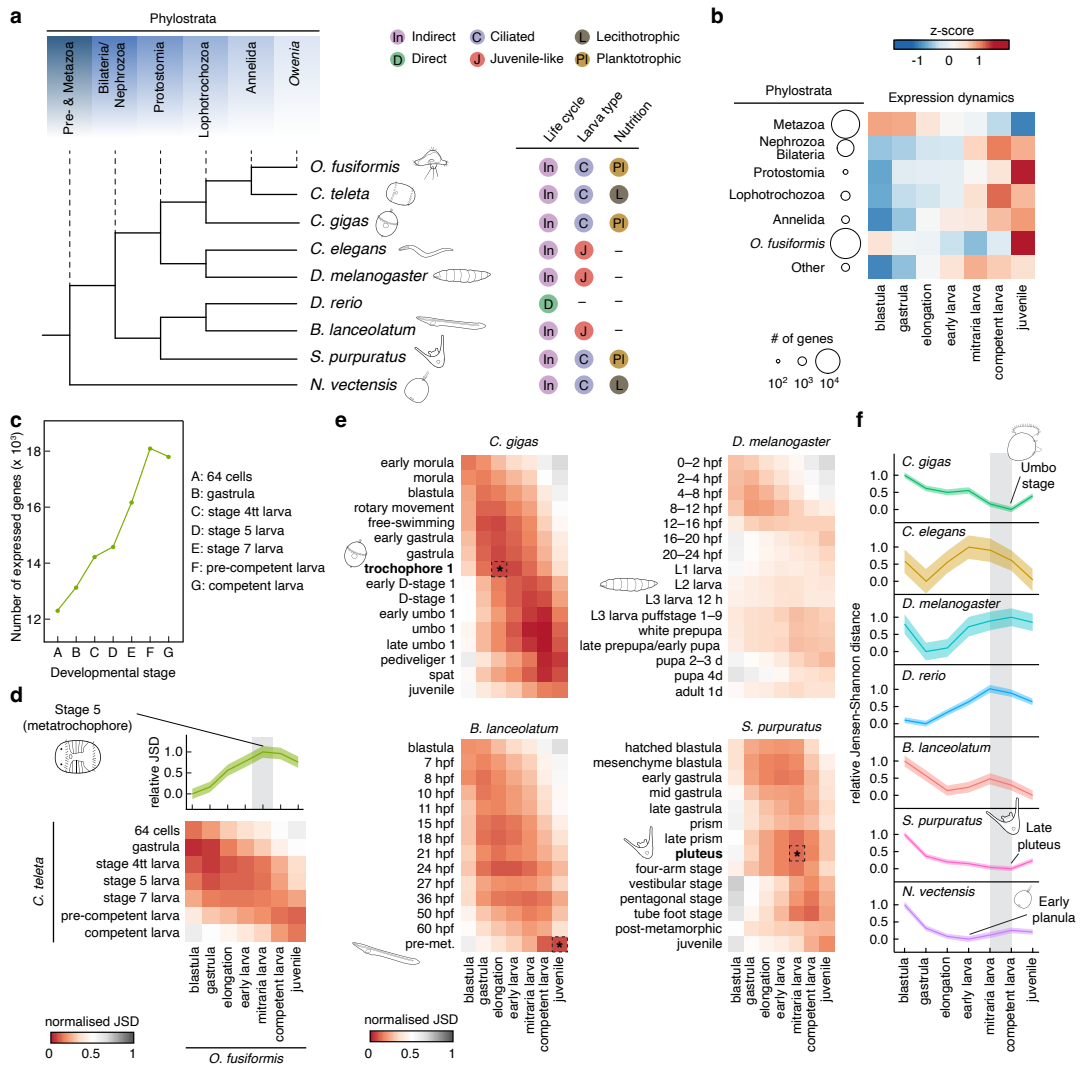
1047 post-larval stage. Clusters 1 (top right) and 6 (bottom right) are the most accessible of each

1048 regulatory programme, and thus are shown enlarged and with predicted bound transcription

1049 factors to the right. Asterisk denotes predicted factors from GimmeMotif curated databases.

1050





1051

1052 **Figure 4 | Novel genes and comparative transcriptional dynamics during larval**

1053 **development.** **a**, Cladogram of the species used for comparative transcriptomics analyses,  
 1054 indicating on top the phylogenetic age of each phylostrata considered for phylostratigraphy.

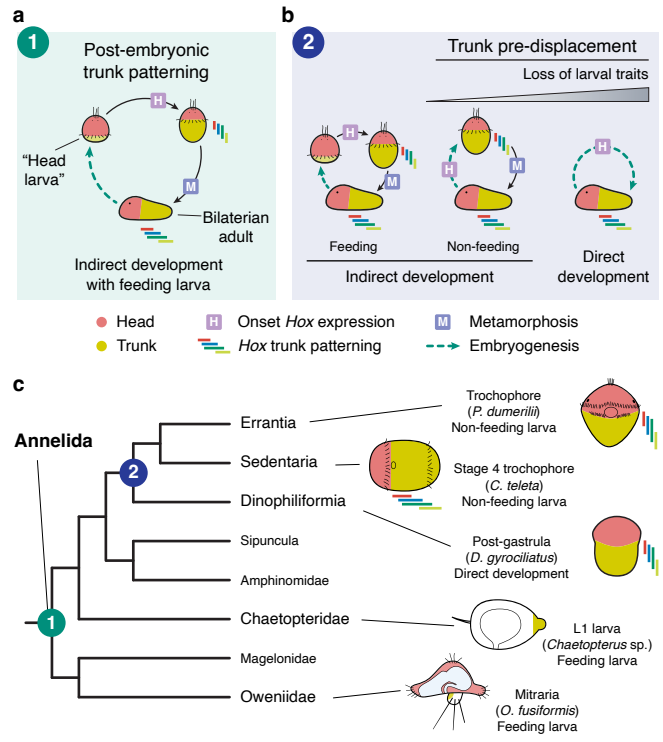
1055 For each species, the type of life cycle (direct/indirect), larval type (ciliated/juvenile-like) and  
 1056 larval nutritional mode (planktotrophic/lecithotrophy) are shown on the right. **b**, Expression

1057 dynamics of each phylostratum by developmental stage, calculated from the 75 % percentile  
 1058 of a quantile-normalised matrix of gene expression levels. Earlier stages are enriched in

1059 metazoan genes, and *O. fusiformis*-specific genes reach their maximum expression levels at  
 1060 the juvenile stage. **c**, Number of expressed genes across *C. teleta* development. **d**, Heatmap of

1061 pairwise normalised transcriptomic Jensen–Shannon Divergence (JSD) between *O. fusiformis*

1062 and *C. teleta*, with the relative JSD of the *C. teleta* stages of minimal divergence to each  
1063 *O. fusiformis* stage on top. **e**, Heatmaps of pairwise normalised JSD between *O. fusiformis*  
1064 and *C. gigas*, *D. melanogaster*, *B. lanceolatum* and *S. purpuratus* (the asterisk indicates the  
1065 stage of minimal JSD between the larval stage of each species with *O. fusiformis*). **f**, Relative  
1066 JSD from stages of minimal divergence of species in **(a)** to each *O. fusiformis* developmental  
1067 stage. Confidence intervals in **(b)** and **(f)** represent the standard deviation from 250 bootstrap  
1068 resamplings of the one-to-one orthologs.



1069

1070 **Figure 5 | Heterochronic shifts in trunk patterning underpin larval evolution in**

1071 **Annelida. a**, Schematic drawing of the life cycle and patterning events in a bilaterian with

1072 indirect development with a feeding larva like the annelid *O. fusiformis*. Embryogenesis

1073 results in a larva with mostly anterior ectodermal fates from which larval organs and the adult

1074 head forms. The onset of trunk differentiation and *Hox* gene expression occurs later, with

1075 larval growth pre-metamorphosis. **b**, Schematic drawings of the three main types of life

1076 cycles and the timing of *Hox* gene expression in bilaterians. Compared to indirect

1077 development with feeding larvae, lineages with non-feeding larvae and direct development

1078 pre-displace (i.e., initiate earlier) trunk differentiation and *Hox* gene expression. Larval

1079 organs are reduced in non-feeding larvae and absent in direct development. **c**, Proposed

1080 evolutionary scenario for larval and life cycle evolution in Annelida. The early branching

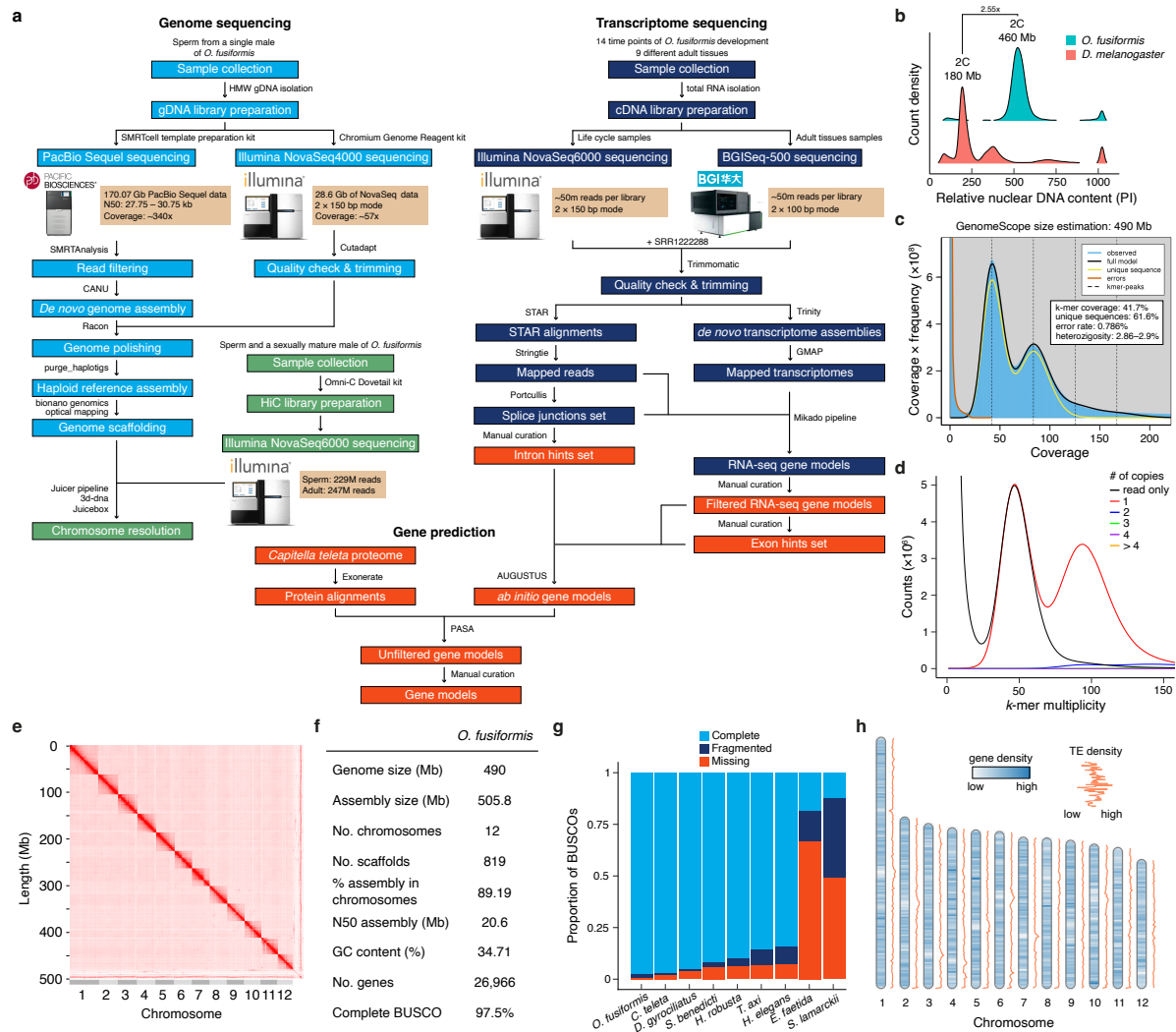
1081 lineages Oweniid and Chaetopteridae exhibit feeding larvae that originally develop with

1082 reduced trunk regions. However, non-feeding larvae in Errantia and Sedentaria (e.g., those of

1083 *P. dumerilii* and *C. teleta*, respectively) already exhibit a patterned trunk region, which is

1084 established post-gastrulation, as in the direct developer *D. gyrociliatus*. Notably, feeding  
1085 larva in Errantia and Sedentaria behave as those of Oweniidae and Chaetopteridae, and thus a  
1086 post-embryonic trunk patterning is likely an ancestral condition (green circle with 1) and the  
1087 convergent pre-displacement of trunk differentiation to embryogenesis (blue box with 2)  
1088 concurred with the evolution of indirect development with feeding larva and direct  
1089 development. Drawings are not to scale.

1090



1091

1092 **Extended Data Figure 1 | Genome sequencing, assembly, and annotation. a**, Flow charts

1093 summarising genome (light blue) and transcriptome sequencing (dark blue), chromosome-

1094 level scaffolding (green) and gene prediction (red). **b**, Flow cytometry estimation of

1095 *O. fusiformis* genome size by comparison of its propidium iodide (PI)-stained nuclear DNA

1096 content against *Drosophila melanogaster*. **c**, GenomeScope 2.0 profile and *k*-mer based

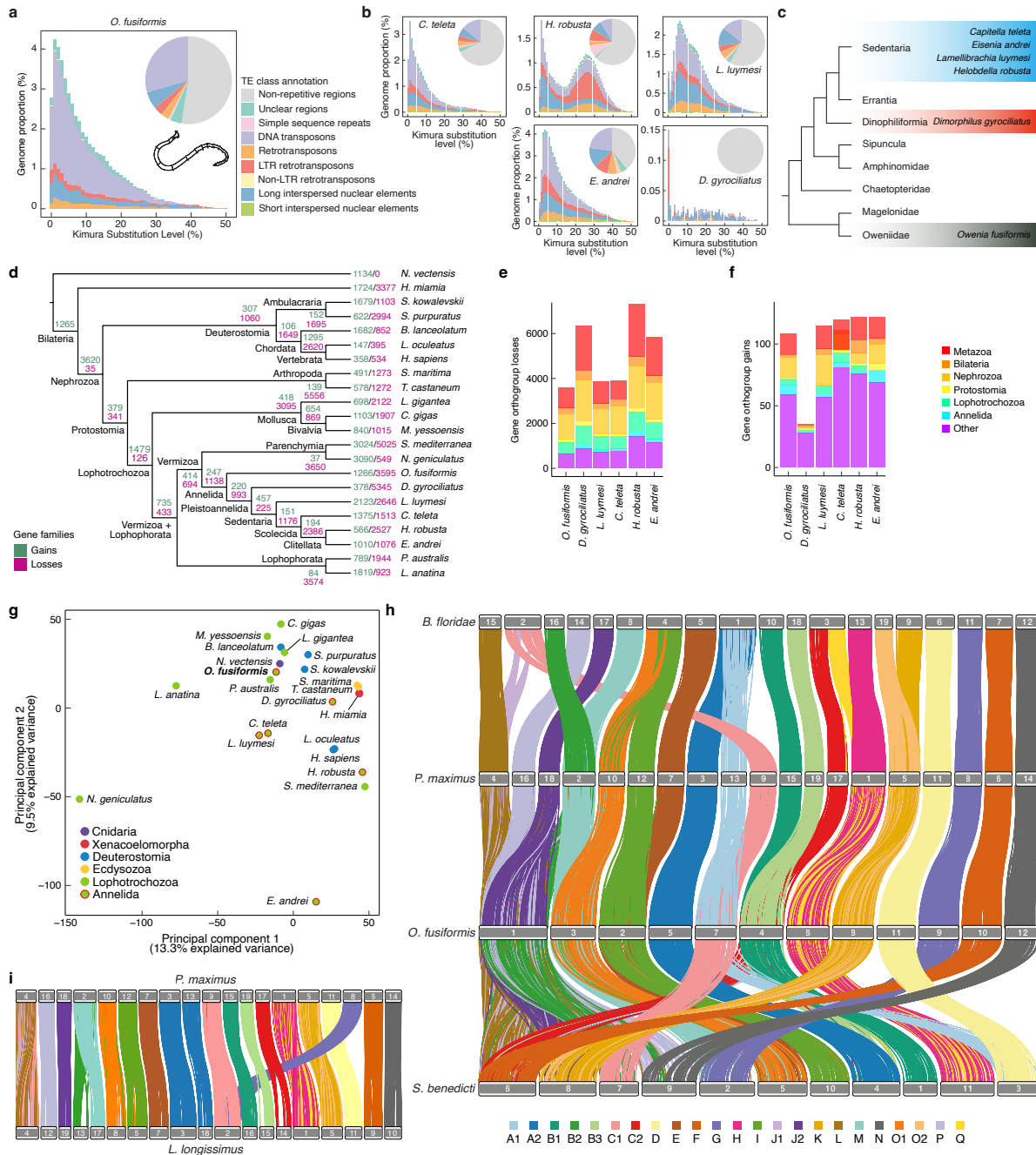
1097 genome size estimation. **d**, *k*-mer distribution plot indicates the nearly complete de-

1098 haploidisation of the reference genome assembly. **e**, Heatmap of HiC contacts showing the

1099 inferred twelve chromosomes of *O. fusiformis*. **f**, Genome assembly and annotation

1100 statistics. **g**, Comparison of metazoan BUSCO values of selected annelid genomes. **h**, Gene

1101 and transposable element (TE) density over the inferred karyotype of *O. fusiformis*.



1102

1103 **Extended Data Figure 2 | The genome of *Owenia fusiformis* is conservatively evolving.**

1104 **a, b**, Pie charts of the transposable element content and Kimura substitution plots of

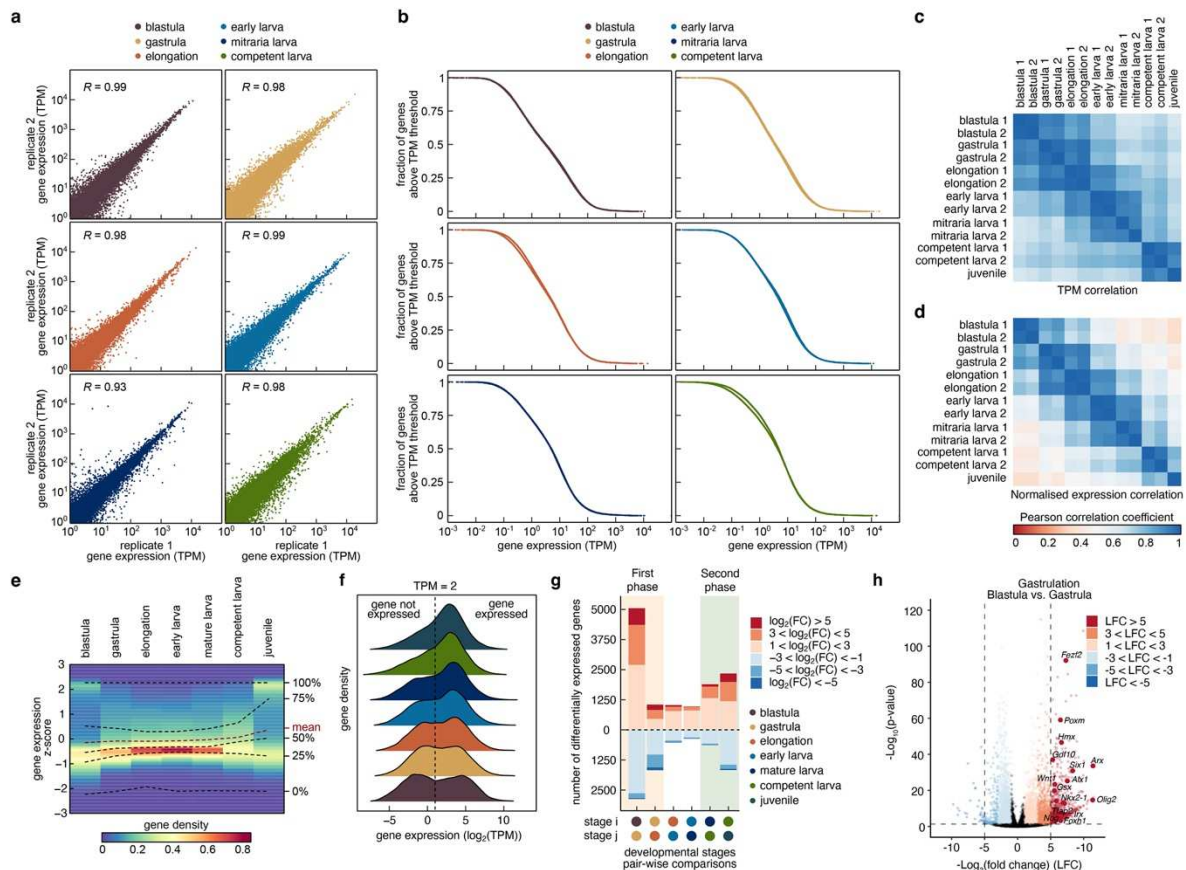
1105 transposable element divergence for *O. fusiformis* and other selected annelid species

1106 belonging to different annelid clades as depicted in **c**. Unlike *H. robusta* and *L. luymesii*,

1107 which show bursts of transposable elements, *O. fusiformis* shows more steady rates of

1108 expansion. **d**, Gene family evolution analysis across 22 metazoan lineages under a consensus

1109 tree topology. Gains are shown in green, losses in violet. Gene family losses in *O. fusiformis*  
1110 are like those of slow-evolving lineages. **e, f**, *O. fusiformis* has the lowest number of gene  
1111 losses of all sampled annelids (**e**), and the least gene expansions (**f**) after the extremely  
1112 compact genome of *D. gyrocolatus*. **g**, Principal component analysis from Fig. 1f, showing  
1113 the full set of species. **h**, Macrosynteny analysis between *O. fusiformis*, and from top to  
1114 bottom, the cephalochordate *Branchiostoma floridae*, the bivalve *Pecten maximus*, and the  
1115 annelid *Streblospio benedicti*. *Owenia fusiformis* retains ancestral linkage groups but also  
1116 exhibits annelid- and species-specific chromosomal arrangements. However, the karyotype of  
1117 *O. fusiformis* is more conserved than that of the annelid *S. benedicti*. **i**, Macrosynteny analysis  
1118 between the bivalve *P. maximus* and the nemertean worm *L. longissimus*.  
1119 *Lineus longissimus* exhibits conserved ancestral bilaterian linkage groups, including three  
1120 potential lophotrochozoan-specific chromosomal rearrangements (H+Q, J2+L and K+O2),  
1121 plus a nemertean-specific fusion (G+C1).



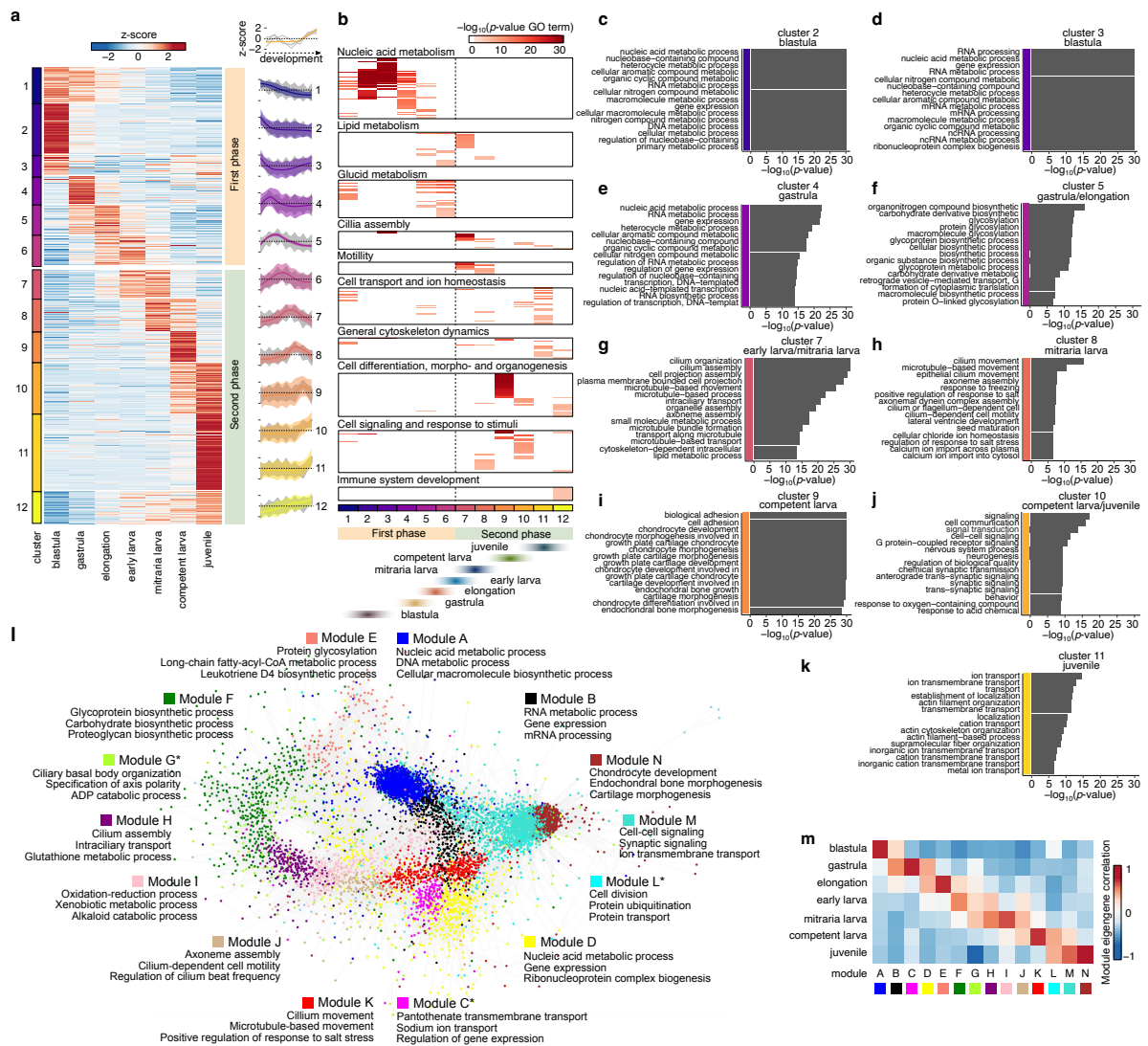
1122

1123 **Extended Data Figure 3 | Gene expression dynamics during *O. fusiformis* development.**

1124 Pairwise scatterplots (a) and pairwise cumulative frequency plots (b) of gene expression  
 1125 levels in transcripts per million (TPM) between biological replicates. *R*: Pearson correlation  
 1126 coefficient. c, d, Correlation matrices between RNA-seq experiments, calculated from a  
 1127 matrix of gene expression levels in TPM (c) and a variance stabilising-transformed matrix of  
 1128 the normalised DESeq2 matrix (d). The satisfactory agreement between biological replicates  
 1129 and an apparent continuum of the developmental transcriptional dynamics can be noted in  
 1130 both matrices. e, Gene expression density heatmap, portraying the normalised gene  
 1131 expression (z-score) during *Owenia* development. Dotted black lines represent 0%, 25%,  
 1132 50%, 75% and 100% quantiles of gene expression. Dotted red line denotes the mean gene  
 1133 expression. As development progresses, gene expression levels increase, with an inflexion  
 1134 point around the early larva stage. f, Ridgeline plot of the distribution of genes by gene  
 1135 expression levels used to experimentally defined a cut-off value of TPM = 2 to deem a gene



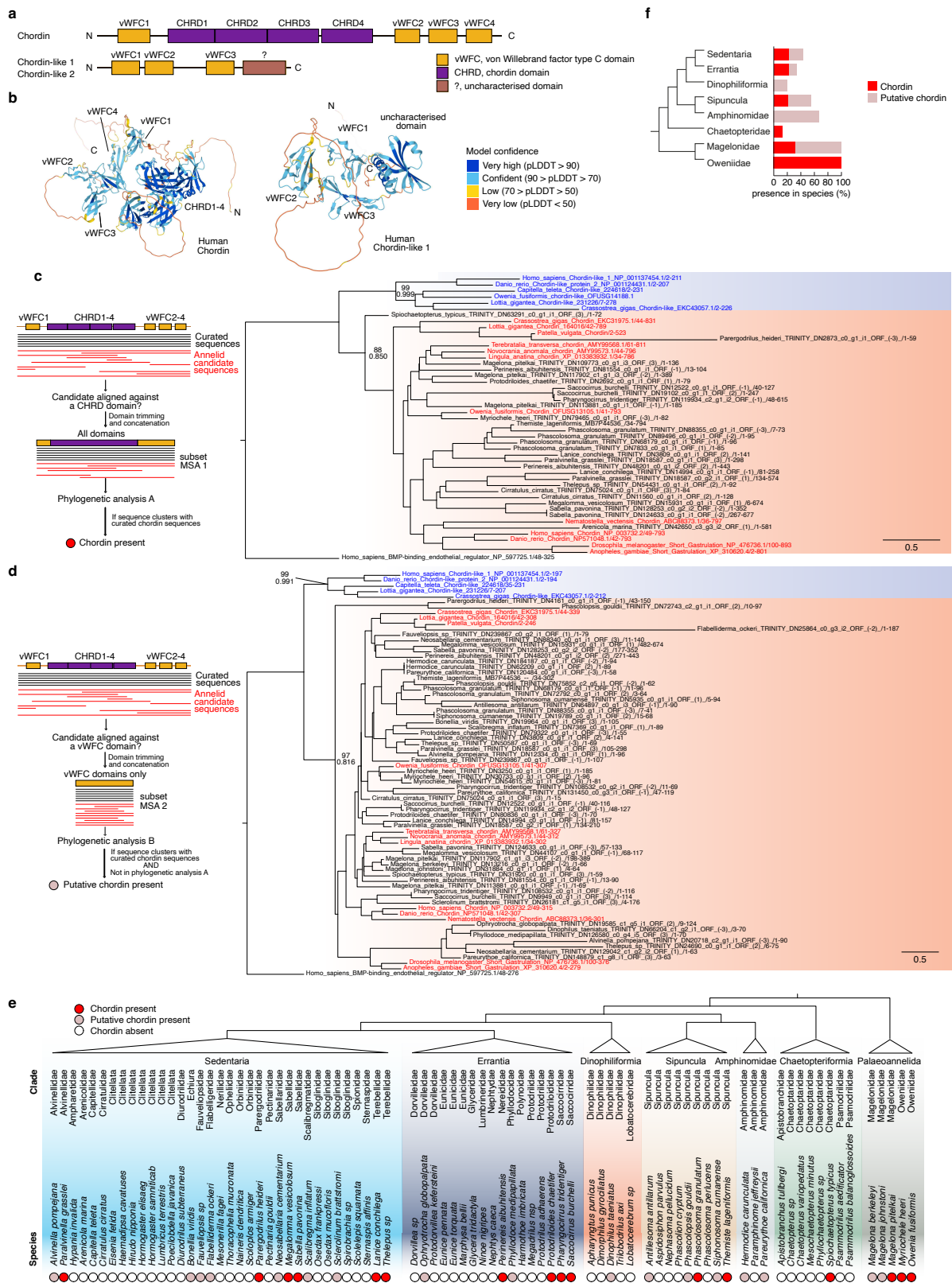
1136 expressed. Colour legend is next to **g**. **g**, Summary of differential gene expression analyses  
1137 between consecutive developmental stages. Only significantly differentially expressed (i.e.,  
1138 those with an adjusted  $p$ -value  $< 0.05$ ) are shown.  $\log_2(\text{FC})$ :  $\log_2(\text{fold-change})$ . **h**, Volcano  
1139 plot of gastrulation (onset of the first transcriptional phase), highlighting top upregulated  
1140 axial patterning genes. Colours of dots represent  $\log_2(\text{FC})$  levels as in (**g**).



1141

1142 **Extended Data Figure 4 | Gene clustering and co-expression network analyses.** **a**, Soft  
 1143 clustered heatmap of all 31,678 transcripts whose expression was not null in at least one  
 1144 developmental stage into an optimal number of 12 clusters. On the right, gene-wise  
 1145 expression dynamics (grey lines) and locally estimated scatterplot smoothing (coloured lines)  
 1146 for each cluster. Coloured shaded areas represent standard error of the mean. **b**, Enrichment  
 1147 analysis of Biological Process gene ontology (GO) terms for RNA-seq clusters. Each line  
 1148 represents a single GO term, for which the  $-\log_{10}(p\text{-value})$  for each RNA-seq cluster is  
 1149 shown in a colour coded scale. Dotted vertical line depicts the inflexion point between the  
 1150 first and second transcriptional phases and the approximate developmental stage  
 1151 corresponding to each cluster is to the bottom. **c-k**, Bar plots representing  $p$ -values of top 15

1152 enriched GO terms in nine representative clusters. For the full list of GO terms and clusters,  
1153 see Supplementary Fig. 2. **i**, Force-directed layout representation of the weighted gene co-  
1154 expression network analysis (WGCNA). For visualisation purposes, only the nodes and edges  
1155 of a random selection of 30% of the transcripts of *O. fusiformis* are depicted here. For each of  
1156 the 14 modules, representative enriched GO terms are shown (full lists are in Supplementary  
1157 Fig. 4). Unadjusted  $p$ -values of GO terms from modules flagged with an asterisk (\*) were  
1158 lower than average. **m**, WGCNA module eigengene correlation with each developmental  
1159 stage of *O. fusiformis*.

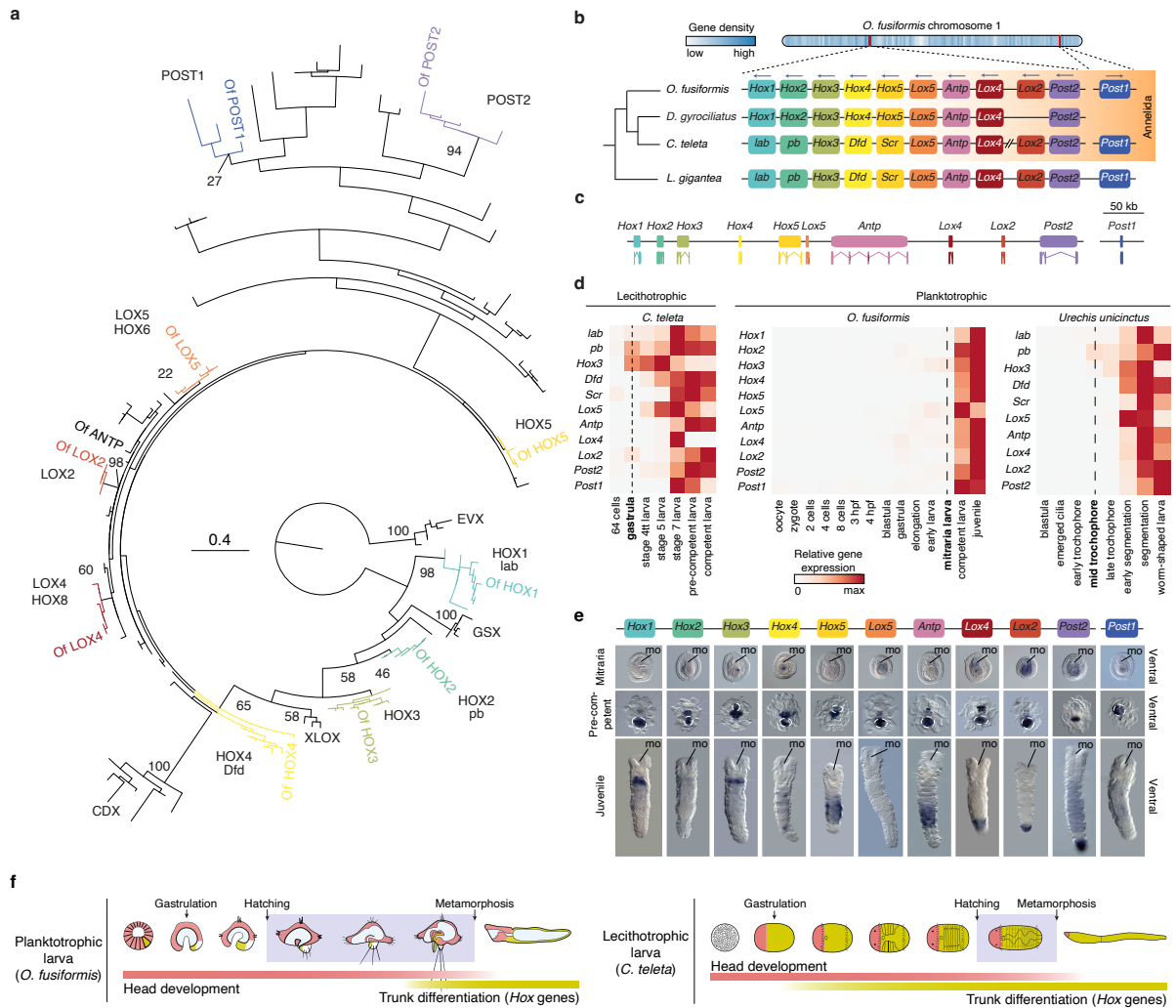


1160

1161 **Extended Data Figure 5 | *chordin* was lost multiple times in annelid lineages. a, Domain**

1162 **organisation of Chordin (CHR) and Chordin-like (CHRDL1/2) proteins, as inferred from**

1163 human orthologs. **b**, AlphaFold protein structure prediction for human Chordin (UniProt:  
1164 Q9H2X0) and Chordin-like 1 (UniProt: Q9BU40) revealed a previously unknown and  
1165 uncharacterised domain in CHRDL1 (also depicted in **a**). **c**, **d**, Orthology assignment of  
1166 *chordin* annelid candidates. From the multiple sequence alignment, candidate annelid  
1167 sequences with a 10-residue or longer fragment aligned against either the CHRDL (**c**; i.e., bona  
1168 fide *chordin* genes) or the vWFC domains (**d**; i.e., putative *chordin* genes) were kept for  
1169 further analysis. CHRDL cluster is shaded in blue; CHRDL cluster, in red. Bootstrap support  
1170 values (top) and posterior probabilities (bottom) are shown at key nodes. Sequences in red  
1171 and blue are curated CHRDL and CHRDL sequences, respectively. **e**, **f**, Summary  
1172 phylogenetic trees of presence/absence of *chordin* (red) or putative *chordin* (light brown)  
1173 across Annelida.

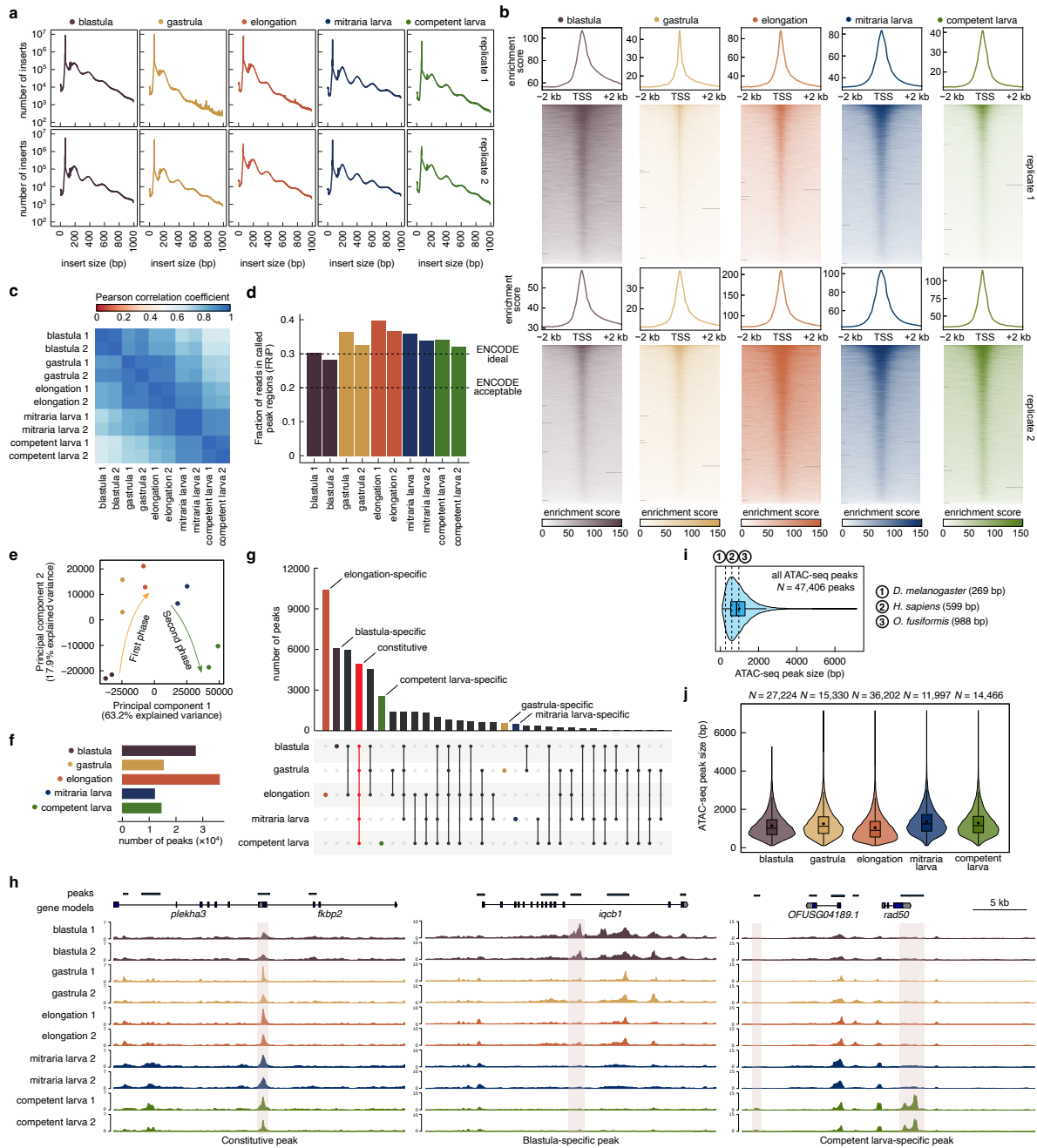


1174

1175 **Extended Data Figure 6 | *Hox* gene complement and expression in *O. fusiformis* and**  
 1176 **other annelid with maximally indirect development. a, Orthology assignment of**  
 1177 ***O. fusiformis* *Hox* genes through maximum likelihood phylogenetic inference. Bootstrap**  
 1178 **support values are shown for major gene groups. Of: *O. fusiformis*. b, Chromosomal location**  
 1179 **of the *Hox* cluster and *Post1* gene in *O. fusiformis* (top) and schematic comparison of *Hox***  
 1180 **cluster organisation in annelids and a mollusc (bottom). c, Schematic representation to scale**  
 1181 **of the genomic loci and intron–exon composition of *Hox* genes in *O. fusiformis*. d, Heatmaps**  
 1182 **of *Hox* gene expression during *C. teleta*, *O. fusiformis* and the echiuran annelid *Urechis***  
 1183 ***unicinctus* development. In the two annelid species with planktotrophic larvae, *Hox* genes**  
 1184 **only become expressed at the larval stage (dotted vertical line) and not during embryogenesis,**

1185 as observed in *C. teleta*. **e**, Whole mount *in situ* hybridisation (ventral views) of *Hox* genes in  
1186 the mitraria, pre-competent, and juvenile stages. The area encircled by a dotted white line at  
1187 the pre-competent stage highlights a region of probe trapping from ingested food content. mo:  
1188 mouth. **f**, Heterochrony model depicting the pre-displacement of trunk differentiation in  
1189 lecithotrophic larvae (as in *C. teleta*) and direct developers, compared to *O. fusiformis* and  
1190 other planktotrophic annelid larvae.

1191



1192

1193 **Extended Data Figure 7 | Chromatin accessibility dynamics during *O. fusiformis***

1194 **development.** **a**, Insert size distribution of ATAC-seq libraries show nucleosomal ladders for  
 1195 all samples. **b**, Heatmaps and summary plots of ATAC-seq enrichment around transcription  
 1196 start sites (TSS;  $\pm 2$  kb) demonstrate at least two-fold enrichment for all samples.

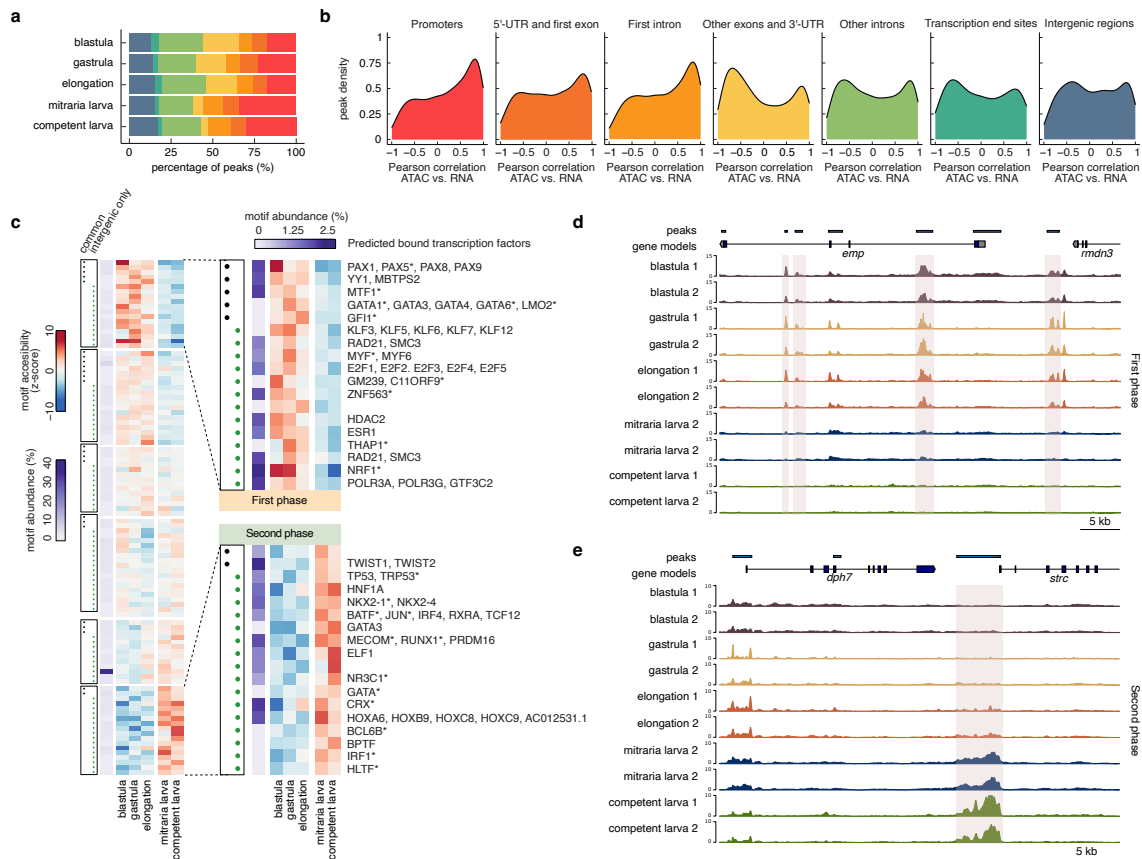
1197 **c**, Correlation matrix based on peak accessibility of the called consensus peak set. **d**, FRiP

1198 scores for ATAC-seq samples indicating acceptable (FRiP = 0.2) and ideal (FRiP = 0.3)

1199 values as per ENCODE standards (dotted lines). **e**, Principal component analysis of ATAC-



1200 seq samples based on peaks as in (c). **f**, Bar plot of ATAC-seq peak number by  
1201 developmental stage. **g**, UpSet plot classification of ATAC-seq peaks by developmental  
1202 stage. Peaks present in more than one stage are coloured in grey. **h**, Representative views of  
1203 constitutive and stage-specific peaks, with the ATAC-seq peak track indicating IDR  
1204 consensus peaks. *plekha3*: pleckstrin homology domain containing A3; *fkbp2*: FKBP prolyl  
1205 isomerase 2; *iqcb1*: IQ calmodulin-binding motif-containing protein 1; *rad50*: RAD50 double  
1206 strand break repair protein. **i**, **j**, Violin plots of ATAC-seq peak width distribution for all peak  
1207 set (**i**) and according to developmental stages (**j**). Dotted lines in **i** represent the mean peak  
1208 size for fruit fly (1), human (2) and *O. fusiformis* (3). Peaks are narrower during axial  
1209 elongation and broader in the mitraria larva.



1210

1211 **Extended Data Figure 8 | Correlation of ATAC-seq and RNA-seq data. a**, Percentage of

1212 ATAC-seq peaks by genomic feature annotation across *O. fusiformis* development. As

1213 development progresses, peaks present in non-first exons and 3'-untranslated regions (3'-

1214 UTRs) become less abundant in favour of peaks located in promoters, first exons and 5'-

1215 UTRs. **b**, Density plots based on the Pearson correlation coefficient between ATAC-seq peak

1216 accessibility and RNA-seq expression level of the nearest gene/transcript to the ATAC-seq

1217 peak. Peaks in promoters and first introns are the most positively correlated with gene

1218 expression, with most other genomic regions displaying a bimodal distribution. **c**, Motif

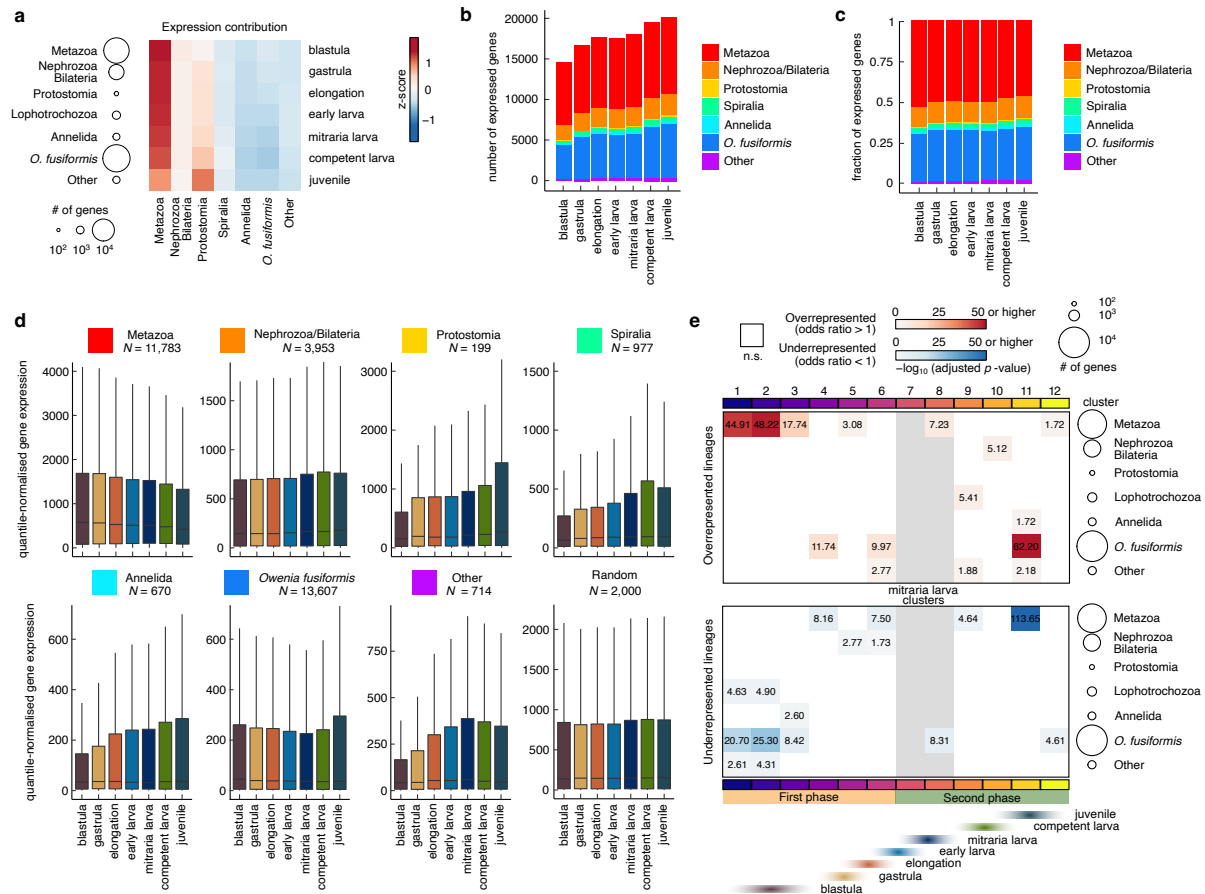
1219 enrichment analysis of intergenic peaks. Clustered heatmap shows the normalised motif

1220 accessibility (z-score), as inferred from chromatin accessibility, and the abundance of the

1221 motif in promoter peaks. Clusters 1 (top right) and 6 (bottom right) are shown in detail as

1222 representative of each regulatory programme. **d**, **e**, Representative peaks associated with each

1223 of the two regulatory programmes highlighted in light red. Peak track corresponds to the  
1224 consensus ATAC-seq peak set. *emp*: epithelial membrane protein-related; *rmdn3*: regulator of  
1225 microtubule dynamics 3; *dph7*: diphthamide biosynthesis 7; *strc*: stereocilin.



1226

1227 **Extended Data Figure 9 | The development of the mitraria larva does not rely on gene**

1228 **novelties.** **a**, Expression contribution of each phylostratum by developmental stage,

1229 calculated from the 75% percentile of a quantile-normalised matrix of gene expression levels.

1230 Metazoan genes are expressed at the highest levels at all stages but the juvenile, at which

1231 genes of protostomian origin take over. **b**, Number and **c**, percentage of expressed genes

1232 throughout development classified by phylostratum, as per Fig. 4a. **e**, Boxplots of quantile-

1233 normalised expression levels of genes classified by phylostratum across *O. fusiformis*

1234 development. **f**, Enrichment analysis of the number of genes per phylostratum in clusters of

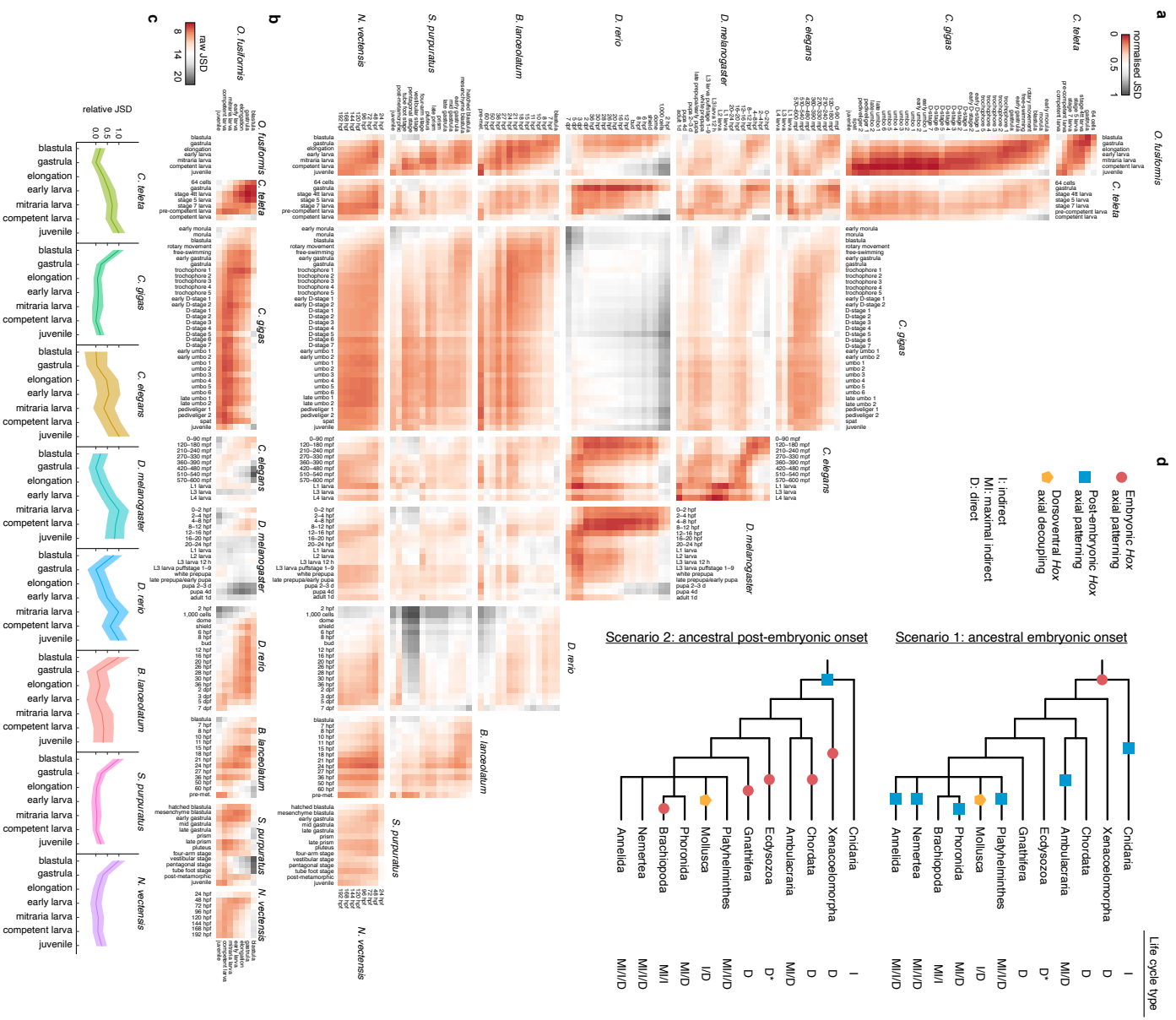
1235 co-transcribed genes as inferred through soft clustering and shown in Extended Data Fig. 4a.

1236 For each cluster and lineage combination, the Bonferroni-adjusted *p*-value of the Fisher's

1237 exact test is shown. The upper table includes significantly overrepresented lineages (odds

1238 ratio, OR > 1, adjusted *p*-value < 0.05) and the lower table includes significantly

1239 underrepresented lineages ( $OR < 1$ , adjusted  $p$ -value  $< 0.05$ ). The results match the  
1240 expression dynamics displayed in **d** (shaded grey are indicates the mitraria stage). In **c** and **f**,  
1241 bubble size is proportional to the number of genes in each phylostratum.



1248 *D. melanogaster*, the bivalve *C. gigas*, and the annelids *O. fusiformis* and *C. teleta*.

1249 **b**, Heatmaps of JSD between *O. fusiformis* and all other eight species using only the subset of  
1250 single copy orthologs common to all nine species. This excludes all genes that are not of pre-  
1251 metazoan and metazoan origin, as they will not be present in *N. vectensis*. **c**, Relative JSD  
1252 from stages of minimal divergence of eight animal species to each *O. fusiformis*  
1253 developmental stage calculated from the subset of single copy common orthologs.

1254 Confidence intervals are the standard deviation from 250 bootstrap resamplings of the single  
1255 copy ortholog subset ( $N = 459$  orthologs for all eight pairwise comparisons). **d**, alternative  
1256 evolutionary scenarios for the deployment of *Hox* genes (as proxy for trunk patterning and  
1257 assuming the staggered expression along the directive axis of cnidarians and anteroposterior  
1258 axis of bilaterians is homologous, which does not necessarily imply homology of the two  
1259 axes). Given our current understanding of *Hox* gene deployment in cnidarian and bilaterian  
1260 taxa (see Supplementary Table 33), a late post-embryonic *Hox* patterning ancestral to  
1261 Bilateria and Cnidaria, as seen in extant lineages with maximal indirect development, is a  
1262 more parsimonious scenario (bottom scenario), which could have been favoured the evolution  
1263 of bilaterian larvae.

1264

## Supplementary Information

1265

### **Annelid functional genomics reveal the origins of bilaterian life cycles**

1266

1267 **Index:**

1268

- **Supplementary Figure 1.** Smudgeplot ploidy estimation.

1269

- **Supplementary Figure 2.** Gene ontology terms enrichment of RNA-seq clusters.

1270

- **Supplementary Figure 3.** Clustering of gene ontology terms enriched in RNA-seq clusters.

1271

1272

- **Supplementary Figure 4.** Gene ontology terms enrichment of WGCNA modules.

1273

- **Supplementary Figure 5.** Full motif enrichment analysis of promoter peaks.

1274

- **Supplementary Figure 6.** Full motif enrichment analysis of intergenic peaks.

1275

- **Supplementary Figure 7.** Quality control and sample correlation of stage-specific RNA-seq samples of *C. teleta*.

1276

1277

- **Supplementary Table 1.** Repetitive elements genome composition in annelids.

1278

- **Supplementary Table 2.** Genomes and annotation files used for the gene family evolution analysis.

1279

1280

- **Supplementary Table 3.** Gene family evolution analysis in 22 metazoan lineages.

1281

- **Supplementary Table 4.** Statistics of gene family evolution analysis.

1282

- **Supplementary Table 5.** Gene family gains in *O. fusiformis*.

1283

- **Supplementary Table 6.** Gene family losses in *O. fusiformis*.

1284

- **Supplementary Table 7.** Analysis of pre- and metazoan orthogroups retention.

1285

- **Supplementary Table 8.** Statistics of RNA-seq libraries for *O. fusiformis*.

1286

- **Supplementary Table 9.** Stage-specific TPM gene expression matrix.

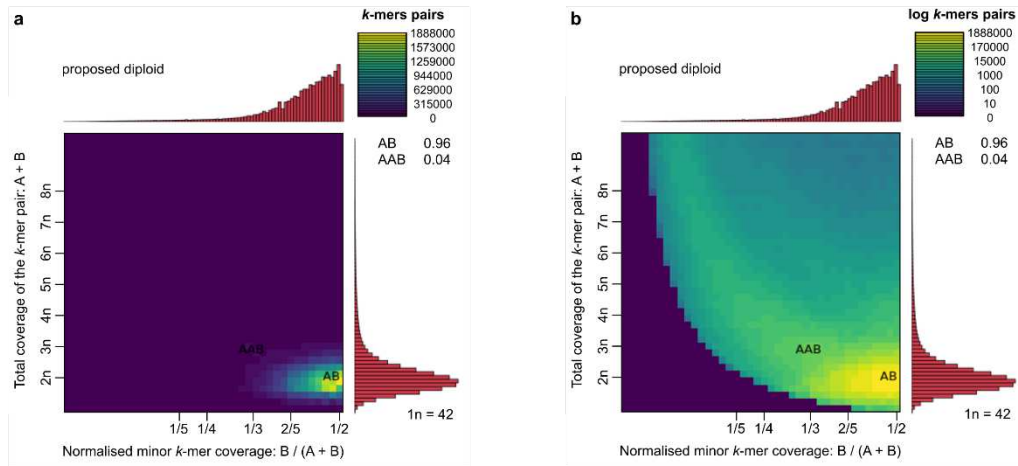
1287

- **Supplementary Table 10.** Stage-specific DESeq2 gene expression matrix.



- 1288 • **Supplementary Table 11.** Genome annotation based on RNA-seq clusters and  
1289 WGCNA modules.
- 1290 • **Supplementary Table 12.** Statistics of gene ontology terms enrichment of RNA-seq  
1291 clusters. Top 30 significant GO terms for each cluster are shown.
- 1292 • **Supplementary Table 13.** Statistics of gene ontology terms enrichment of WGCNA  
1293 modules. Top 15 significant GO terms for each module are shown.
- 1294 • **Supplementary Table 14.** Datasets used for annelid *chordin* mining.
- 1295 • **Supplementary Table 15.** Summary of mutual best hit (MBH) analysis and  
1296 translated peptides for all 104 unique *chordin* annelid candidates.
- 1297 • **Supplementary Table 16.** Curated sequences used for *chordin* orthology assignment.
- 1298 • **Supplementary Table 17.** List of *chordin* annelid candidates, presence or absence in  
1299 phylogenetic analyses A and B, and associated exclusion criteria.
- 1300 • **Supplementary Table 18.** Summary of *chordin* presence/absence across annelids.
- 1301 • **Supplementary Table 19.** Curated sequences used for *Hox* genes orthology  
1302 assignment.
- 1303 • **Supplementary Table 20.** Datasets used for *Hox* gene expression analysis during  
1304 *Urechis unicinctus* development.
- 1305 • **Supplementary Table 21.** Primers used for ATAC-seq library preparation.
- 1306 • **Supplementary Table 22.** Statistics of ATAC-seq experiments.
- 1307 • **Supplementary Table 23.** Normalised stage-wise accessibility, annotation by  
1308 genomic feature and correlation with expression of nearest gene of the consensus  
1309 ATAC-seq peak set.
- 1310 • **Supplementary Table 24.** Normalised stage-wise occupancy of the consensus  
1311 ATAC-seq peak set.
- 1312 • **Supplementary Table 25.** Motif enrichment analysis of promoter peaks.

- 1313 • **Supplementary Table 26.** Motif enrichment analysis of intergenic peaks.
- 1314 • **Supplementary Table 27.** Phylostratigraphic genome annotation.
- 1315 • **Supplementary Table 28.** Statistics for RNA-seq libraries for *C. teleta*.
- 1316 • **Supplementary Table 29.** Developmental RNA-seq time course datasets used for  
1317 comparative transcriptomics.
- 1318 • **Supplementary Table 30.** Single copy ortholog number for all one-to-one  
1319 comparisons between all 9 metazoan lineages.
- 1320 • **Supplementary Table 31.** Stages of minimal transcriptome divergence to each  
1321 *O. fusiformis* stage, calculated from the full single copy ortholog set.
- 1322 • **Supplementary Table 32.** Stages of minimal transcriptome divergence to each  
1323 *O. fusiformis* stage, calculated from the subset of common single copy orthologs.
- 1324 • **Supplementary Table 33.** Literature review on *Hox* genes deployment timing across  
1325 bilaterian lineages.
- 1326 • **Supplementary Tables 34–45.** List of differentially expressed genes (DEG) during  
1327 *O. fusiformis* development from pair-wise comparisons between consecutive  
1328 developmental stages. Statistics of DEG analysis, functional annotation, and  
1329 normalised DESeq2 levels of expression are shown for each gene.
- 1330



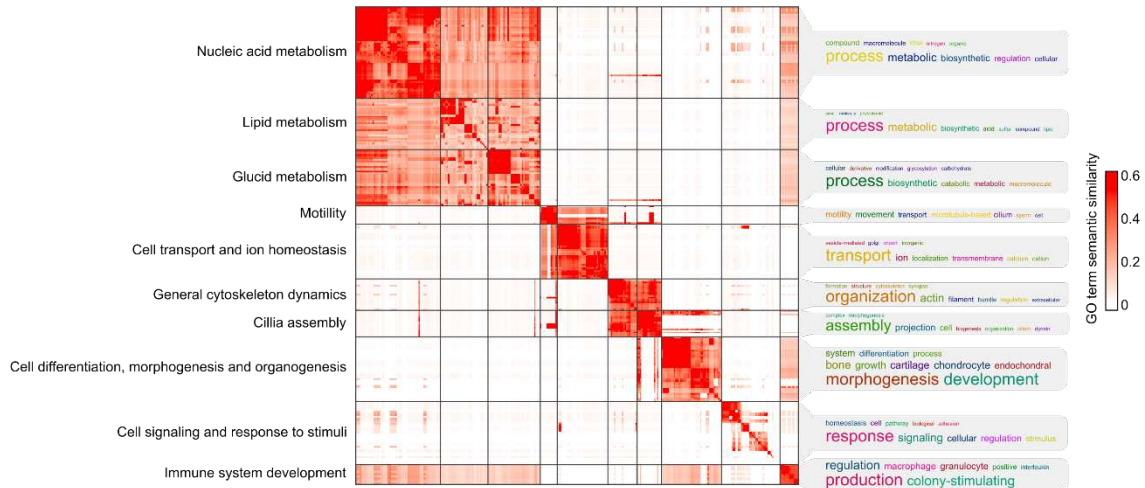
1331

1332 **Supplementary Figure 1 | Smudgeplot ploidy estimation. a**, Linear scale and **b**, base 10

1333 logarithmic scale smudgeplots. Diploid (AB) *k*-mer pairs are predominant (0.96) for

1334 *O. fusiformis* genome, suggesting diploidy.



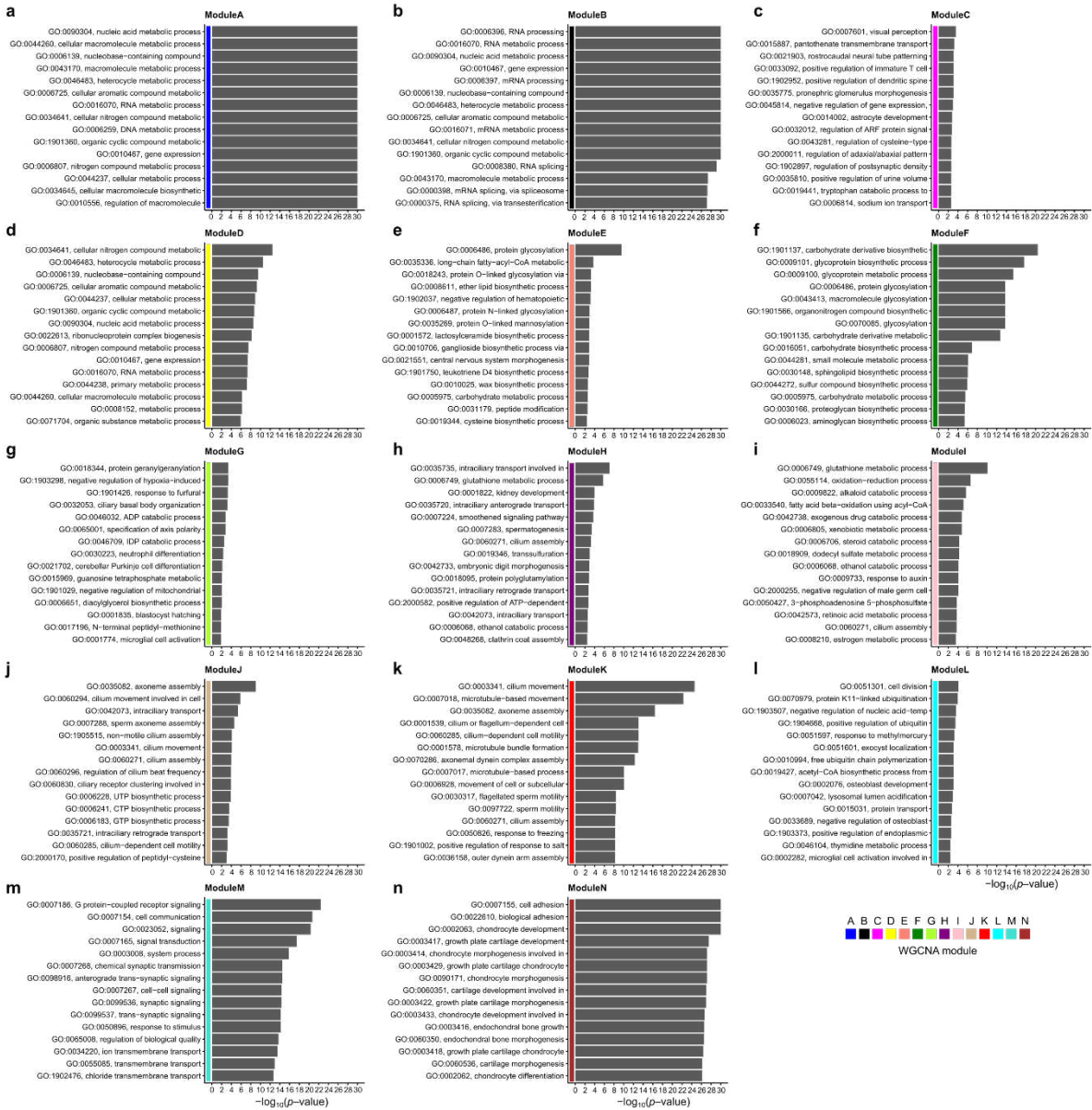


1340

1341 **Supplementary Figure 3 | Clustering of gene ontology terms enriched in RNA-seq**

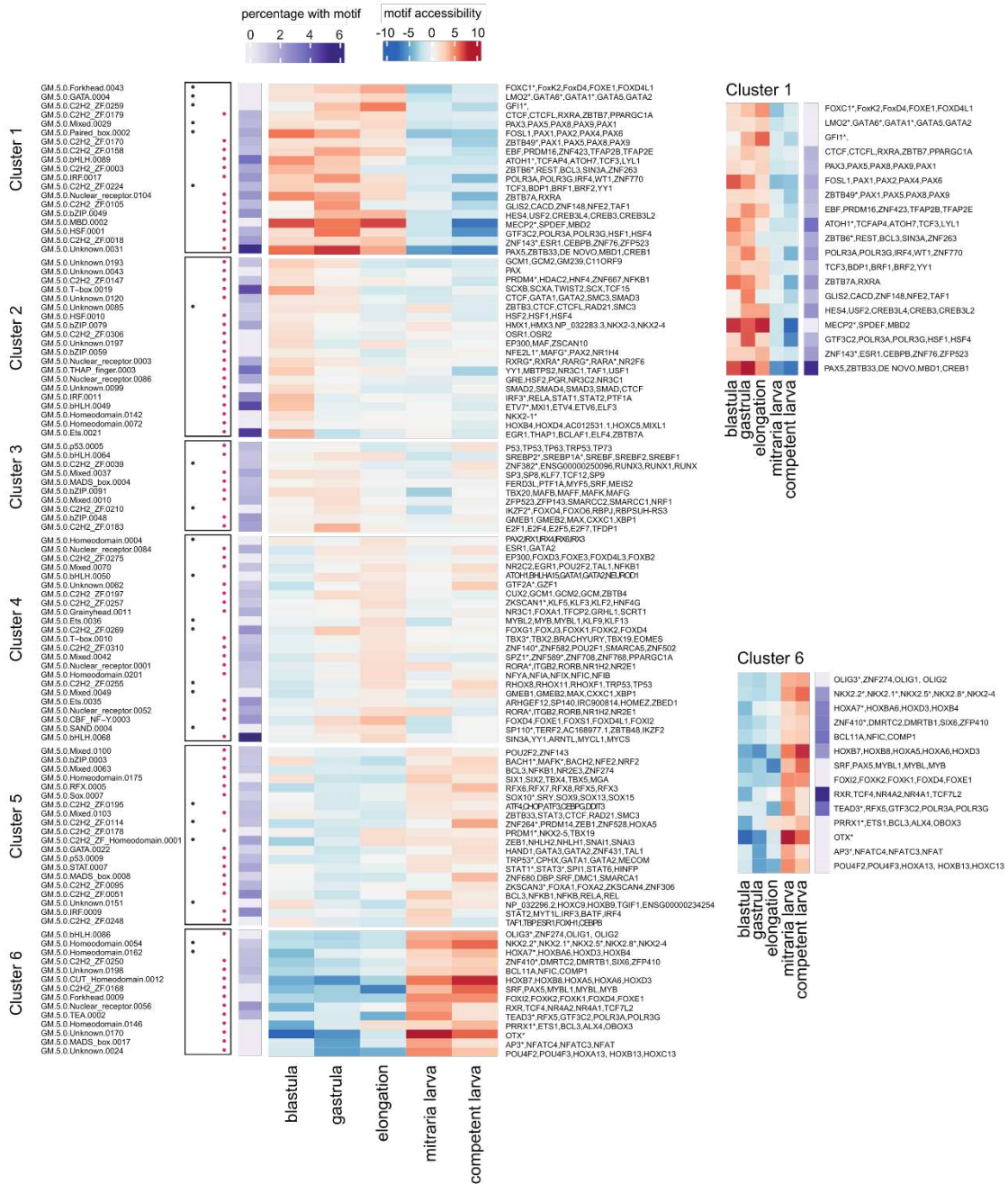
1342 **clusters.** Similarity matrix of all 288 non-redundant gene ontology (GO) terms for biological  
 1343 process from the GO term enrichment analysis performed on RNA-seq clusters. GO terms  
 1344 were grouped through *k*-means clustering according to their semantic similarity. A word  
 1345 cloud recapitulates each cluster, with word size being proportional to word frequency in the  
 1346 GO terms contained within that cluster. Custom umbrella terms were selected to summarise  
 1347 each cluster of GO terms, here shown on the left of the matrix.

1348



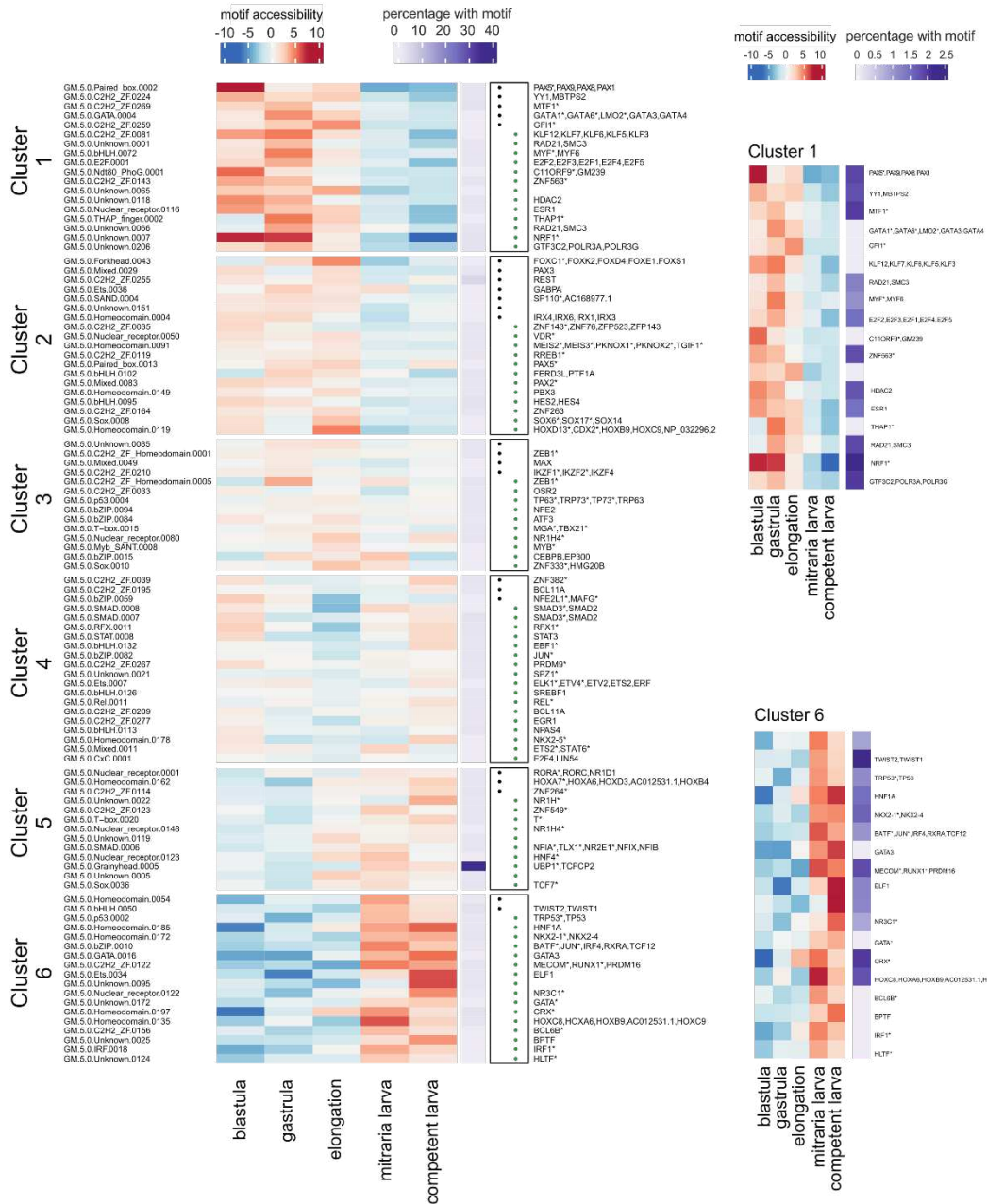
1349

1350 **Supplementary Figure 4 | Gene ontology terms enrichment for WGCNA modules. a-**  
 1351 **n, Barplots depicting unadjusted  $p$ -values of the top 15 gene ontology (GO) terms for**  
 1352 **biological process for each of the 14 modules (A–N, a–n) of co-expressed transcripts**  
 1353 **retrieved through our WGCNA approach.**



1354

1355 **Supplementary Figure 5 | Full motif enrichment analysis of promoter peaks.** Full motif  
 1356 enrichment analysis of promoter peaks. Clustered heatmap shows the normalised motif  
 1357 accessibility (z-score), as inferred from chromatin accessibility, and the abundance of the  
 1358 motif in promoter peaks. Clusters 1 (top right) and 6 (bottom right) are shown in detail as  
 1359 representative of each regulatory programme. The full list of all predicted bound transcription  
 1360 factors and raw motif IDs is shown here.



1361

1362 **Supplementary Figure 6 | Full motif enrichment analysis of intergenic peaks.** Full motif

1363 enrichment analysis of intergenic peaks. Clustered heatmap shows the normalised motif

1364 accessibility (z-score), as inferred from chromatin accessibility, and the abundance of the

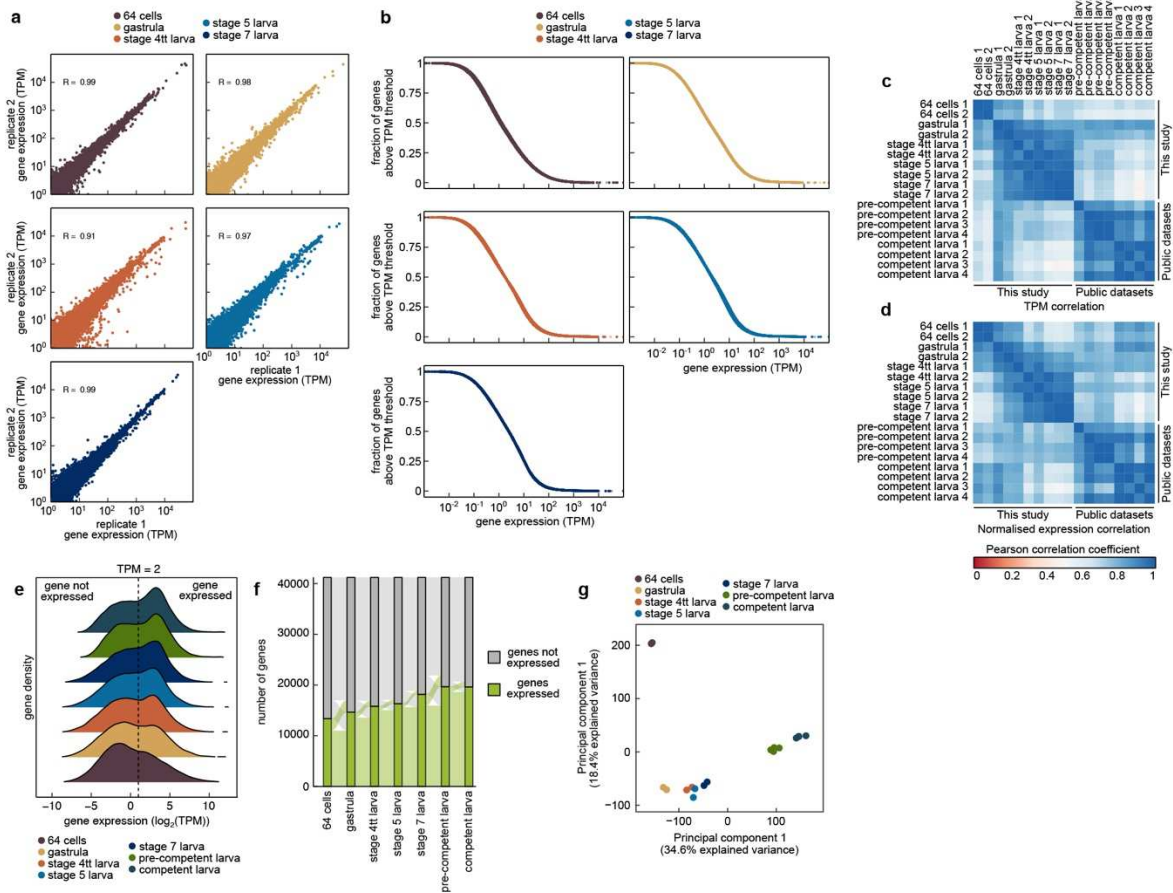
1365 motif in intergenic peaks. Clusters 1 (top right) and 6 (bottom right) are shown in detail as

1366 representative of each regulatory programme. The full list of all predicted bound transcription

1367 factors and raw motif IDs is shown here. Note the scale for motif abundance is different for

1368 zoomed detailed clusters than for the full set, for comparison purposes.





1369

1370 **Supplementary Figure 7 | Quality control and sample correlation of stage-specific RNA-**

1371 **seq samples of *C. teleta*.** Pairwise scatterplots (a) and pairwise cumulative frequency plots

1372 (b) of gene expression levels in transcripts per million (TPM) between biological replicates.

1373 *R*: Pearson correlation coefficient. c, d, Correlation matrices between RNA-seq experiments,

1374 calculated from a matrix of gene expression levels in TPM (c) and a variance stabilising-

1375 transformed matrix of the normalised DESeq2 matrix (d). Adequate agreement between

1376 biological replicates can be observed in both matrices. e, Ridgeline plot of the distribution of

1377 genes by gene expression levels used to experimentally defined a cut-off value of TPM = 2 to

1378 deem a gene expressed. f, Alluvial plot of expressed and not expressed genes throughout the

1379 development of *C. teleta*. As in Fig. 4d, the two phases of gene expression observed for

1380 *O. fusiformis* in Fig. 2c cannot be discerned in *C. teleta*. **g**, Principal component analysis of  
1381 the developmental RNA-seq time course of *O. fusiformis*.

## Supplementary Files

This is a list of supplementary files associated with this preprint. Click to download.

- [LMZSupplementaryTables01.xlsx](#)
- [LMZSupplementaryTables02.xlsx](#)